

## Accepted Manuscript

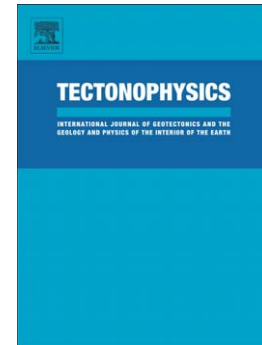
Crustal Anisotropy in Northeastern Tibetan Plateau Inferred from Receiver Functions: Rock Textures Caused by Metamorphic Fluids and Lower-Crust Flow?

Zhen Liu, Jeffrey Park, Danny M. Rye

PII: S0040-1951(15)00433-3  
DOI: doi: [10.1016/j.tecto.2015.08.006](https://doi.org/10.1016/j.tecto.2015.08.006)  
Reference: TECTO 126726

To appear in: *Tectonophysics*

Received date: 15 October 2014  
Revised date: 14 July 2015  
Accepted date: 12 August 2015



Please cite this article as: Liu, Zhen, Park, Jeffrey, Rye, Danny M., Crustal Anisotropy in Northeastern Tibetan Plateau Inferred from Receiver Functions: Rock Textures Caused by Metamorphic Fluids and Lower-Crust Flow?, *Tectonophysics* (2015), doi: [10.1016/j.tecto.2015.08.006](https://doi.org/10.1016/j.tecto.2015.08.006)

This is a PDF file of an unedited manuscript that has been accepted for publication. As a service to our customers we are providing this early version of the manuscript. The manuscript will undergo copyediting, typesetting, and review of the resulting proof before it is published in its final form. Please note that during the production process errors may be discovered which could affect the content, and all legal disclaimers that apply to the journal pertain.

Title: Crustal Anisotropy in Northeastern Tibetan Plateau Inferred from Receiver Functions:  
Rock Textures Caused by Metamorphic Fluids and Lower-Crust Flow?

Authors: Zhen Liu, Jeffrey Park, Danny M. Rye

Affiliations:

Department of Geology and Geophysics, Yale University, New Haven, Connecticut, USA

Abstract

The crust of Tibetan Plateau may have formed via shortening/thickening or large-scale underthrusting, and subsequently modified via lower-crust channel flows and volatile-mediated regional metamorphism. The amplitude and distribution of crustal anisotropy record the history of continental deformation, offering clues to its formation and later modification. In this study, we first investigate the back-azimuth dependence of Ps converted phases using multi-taper receiver functions (RFs). We analyze teleseismic data for 35 temporary broadband stations in the ASCENT experiment located in northeastern Tibet. We stack receiver functions after a moving-window moveout correction. Major features of RFs include: 1) Ps arrivals at 8-10s on the radial components, suggesting a 70-90-km crustal thickness in the study area; 2) two-lobed back-azimuth variation for intra-crustal Ps phases in the upper crust ( $< 20$  km), consistent with tilted symmetry-axis anisotropy or dipping interfaces; 3) significant Ps arrivals with four-lobed back-azimuth variation distributed in distinct layers in the middle and lower crust (up to 60 km), corresponding to (sub)horizontal-axis anisotropy; 4) weak or no evidence of azimuthal anisotropy in the lowermost crust. To study the anisotropy, we compare the observed RF stacks with one-dimensional reflectivity synthetic seismograms in anisotropic media, and fit major features by “trial and error” forward modeling. Crustal anisotropy offers few clues on plateau formation, but strong evidence of ongoing deformation and metamorphism. We infer strong horizontal-axis anisotropy concentrated in the middle and lower crust, which could be explained by vertically

aligned sheet silicates, open cracks filled with magma or other fluid, vertical vein structures or by 1-10-km-scale chimney structures that have focused metamorphic fluids. Simple dynamic models encounter difficulty in generating vertically-aligned sheet silicates. Instead, we interpret our data to support the hypothesis of vertical metamorphic-fluid domains whose alignment is determined by shear motion within the boundary layers of crustal channel flow.

Key words: receiver functions, Tibetan crust, azimuthal anisotropy, metamorphic fluids

## 1. Introduction

The Tibetan Plateau has the largest area of elevated topography on Earth and is widely considered to be the result of India-Eurasia collision starting ~50 Ma (e.g. Allegre et al., 1984; Yin and Harrison, 2000). The plateau is bounded by the Kunlun Fault in the north and the Indus-Zangbo Suture in the south, and consists of microplates, namely the Lhasa, Qiangtang and Songpan-Ganzi terranes, separated by the Bangong-Nujiang and Jinsha sutures. Due to its complex deformation history, the formation and evolution of the plateau remain in debate. Various formation models have been proposed, such as underthrusting of the Indian Plate (e.g. Zhao and Morgan, 1987; Jackson et al., 2008), underthrusting of the Asian Plate (e.g. Willett and Beaumont, 1994; Kind et al., 2002; Gray and Pysklywec, 2012), and crustal shortening and thickening (e.g. Dewey et al., 1988, England and Houseman, 1989). After formation, crustal flow (e.g. Royden et al., 1997; Clark and Royden, 2000; Klemperer, 2006) mediates plateau spreading and collapse. In addition to kinematic flow effects, regional-scale metamorphism can generate foliation, veining and juxtaposed metasomatized lithologies that generate an effective anisotropy (Shea and Kronenberg, 1993; Volland and Kruhl, 2004; Connolly and Podladchikov, 2013).

Geophysical observations have provided useful constraints on the geodynamic evolution of the plateau. Seismic-velocity structures beneath Tibet using seismic tomography and receiver functions (RFs) have been inferred by Kind et al., (1996), Xu et al. (2007), Yao et al. (2008), Li et al. (2009), Guo et al. (2009), Acton et al. (2010), Yang et al. (2010; 2012), and Jiang et al. (2011). Consistently, the crustal models indicate mid-crustal low-velocity zones (LVZs) across most of Tibet. In addition, magnetotelluric studies have imaged highly conductive zones in the mid-to-lower crust in northern and eastern Tibet (Unsworth et al., 2004; Bai et al., 2010). Both seismic velocity and electrical resistivity can be reduced by increased temperature or the presence of fluids. The observations imply that the deep Tibetan crust has weakened (Kirby, 1984), and ductile shear zones or channel flows could occur (Klemperer, 2006; Yang et al., 2012). Thus,

finding evidence of crustal deformation is key to improving our understanding of the plateau history.

One of the most powerful approaches to trace deformation processes is by detecting seismic anisotropy (e.g. Park and Levin, 2002; Long, 2013). Anisotropy in seismic-wave propagation can be caused by various conditions, such as aligned cracks, periodic layering, parallel fractures, preferred orientation of mineral grains and metamorphic foliation. The anisotropy of each rock texture can be approximated, to first order, by hexagonal symmetry (transverse isotropy). In Tibet, shear-wave splitting shows various fast-polarization patterns in different areas (McNamara et al., 1994; Huang et al., 2000; Lev et al., 2006). The birefringence of S waves has typically been interpreted with the lattice-preferred orientation (LPO) of upper-mantle minerals, such as olivine. In terms of Tibetan crust, strong radial anisotropy has been detected in the mid-to-lower crust (Shapiro et al., 2004; Duret et al., 2010; Huang et al., 2010; Xie et al., 2013). Radial anisotropy assumes a transverse-isotropic symmetry with a vertical symmetry axis, where horizontally and vertically polarized shear waves travel at different speeds. In contrast, azimuthal anisotropy requires a horizontal or tilted symmetry axis such that seismic velocities vary as a function of incoming wave direction. Observations of azimuthal anisotropy, therefore, are needed to infer the lateral shear predicted by geodynamic models for the plateau.

Azimuthal anisotropy has been investigated in different locales using receiver functions (e.g. Levin and Park, 1997a; Peng and Humphreys, 1997; Savage 1998; Frederiksen and Bostock, 2000; Levin and Park, 2000; Park et al., 2004; Savage et al., 2007; Wirth and Long, 2012; 2014). RF analysis detects interfaces with sharp velocity contrasts beneath the seismic station. Assuming that source and path effects are embedded within the vertical component of the P-wave coda, the deconvolution of horizontal components from the vertical component produces radial RFs and transverse RFs. Radial RFs are sensitive to isotropic seismic structure. Transverse RFs are

sensitive to anisotropic layering and/or a dipping interface. Analysis involving both radial and transverse component will provide a good estimate of seismic structure.

In central and eastern Tibet, crustal anisotropic or dipping structures have been detected by RF-waveform modeling (Sherrington et al., 2004; Ozacar and Zandt, 2004). Alternatively, an average azimuthal anisotropy of the crust can also be estimated by harmonic analysis of the Moho Ps arrival time (Liu and Niu, 2012) to determine its birefringence. Sun et al (2012) observed significant anisotropy with 0.5s-0.9s birefringence time in the southeastern Tibetan crust. In their study, this birefringence was associated with 6% anisotropy distributed evenly in the lower crust. However, seismic anisotropy may exist in single or multiple crustal layers rather than throughout the lower crust. Levin and Park (1998) demonstrated that Ps converted waves from the top and bottom of a thin shear zone would mimic the effect of Ps birefringence in a uniformly-strained crust. It is important to determine how seismic anisotropy is distributed through the crust. A crust composed of thin shear zones would be preferred over evenly-distributed anisotropy if Ps converted phases with harmonic back-azimuth variations are generated at many levels within the crust. Shiomi and Park (2008) extracted the back-azimuth harmonics of both radial and transverse RFs as a function of the incoming P-wave direction, suggesting thin anisotropic layers along dipping interfaces beneath the Kii peninsula above the Nankai subduction zone.

In this study, we apply the harmonic-decomposition technique (Shiomi and Park, 2008; Bianchi et al., 2010) to 35 stations of the ASCENT temporary network (Yang et al., 2012) in northeastern Tibet. Harmonic stacks of RFs from these stations offer strong evidence for layered seismic anisotropy through much of the thick Tibetan crust, consistent with complex deformation. Because the RF-stacks of most stations share common features in the arrival times of anisotropic signals, we run trial-and-error forward modeling on five selected stations with the most clear and robust RF-signals that can be interpreted most readily with simple layered models. In the current paper, combining individual RFs from neighboring stations is not performed due to the weak

clustering of the mid-crust piercing points. In this dataset, neighboring stations are typically separated by ~40-55 km. For two stations separated by 40 km to share a common conversion point at mid-crustal depth (~ 30 km), a phase velocity of ~6.3 km/s is needed (assuming  $V_s = 3.5$  km/s), which is too low for teleseismic waves.

In the following sections, we will show the results from the analysis after a description of the data and harmonic-stacking methods. The Discussion ponders the geophysical implications of our receiver-function stacks. Many crustal processes can generate anisotropy, and we argue that the geometry of anisotropy can be used to select between options. In particular, we interpret the RFs to reveal two shear zones that bound a lower-crust that flows away from the north-converging Indian plate. We argue that the anisotropy that we infer for these shear layers has geometry that does not comport with plausible lattice-preferred orientation (LPO) of sheet-silicate minerals, whose slow-axes of symmetry ought to dominate the LPO (Shea and Kronenberg, 1993; Okaya and Christensen, 2002). We argue instead for anisotropic rock textures caused by veining, cracking, channelized metasomatism or other macroscopic processes. These processes associated with regional metamorphism have been invoked to explain lower-crust exposures of older continental collisions (McLelland, 1984; Bohlen et al, 1985; Valley et al., 1990; Ague, 1995; 2003; Connolly and Podladchikov, 2004; Dorr and Zulauf, 2010), and are plausibly active within the deep crust of Tibet. Finally, we observe that the lowermost layer of the crust has mafic  $V_p$  (~7 km/sec) and lacks strong anisotropy. We suggest that this mafic layer has not underthrust laterally along the Moho, but has formed in place as a mafic granulite, either via ponded melts from the mantle (Fountain, 1989) or via intense metamorphism of Tethyan dolomitic and pelitic sediments (Orville, 1969; Ague, 2003).

## 2. Data and Method

### 2.1 Data

We compute RFs using three-component seismic data from ASCENT network (and station CBNAQ) in northeastern Tibet (Fig. 1). Ground motion was sampled at 25-Hz. We chose 35 stations with available data from 2007 (or 2008) to 2009, which provides good back-azimuth coverage. We selected teleseismic events (epicentral distance  $30^\circ < \Delta < 100^\circ$ ) with  $M > 5.5$  to ensure a high signal to noise ratio (Fig. 2).

### 2.2 Methods

#### 2.2.1 Receiver functions processing

Receiver functions are estimated in the frequency domain from multiple-taper spectrum estimates (Park and Levin, 2000). Multi-taper spectrum estimates balance resistance to spectral leakage against spectral information in a fixed bandwidth (Thomson 1982; Park et al., 1987). To derive RFs, the E and N horizontal components of seismic records are rotated to the radial-transverse (R-T) system. We high-pass the seismic records at  $f=0.03$  Hz to eliminate long-period drift and to select data with high signal-to-noise ratio. We use a time-bandwidth product of  $p=2.5$  and apply the first three eigentapers to the first 80 seconds of the original data series to compute three “eigenspectra” that are statistically uncorrelated. We deconvolve the R and T time series from the Z (vertical component) time series via a least-squares correlation between their eigenspectra. Multitaper correlation is more stable than spectral division in the frequency domain (Park and Levin, 2000), and does not require water-level damping with real data. Uncertainties are estimated from the coherence between horizontal and vertical components (Park and Levin, 2000). Finally, we compute time-domain RFs by applying the inverse Fast Fourier Transform (FFT) to the frequency-domain RFs. To achieve a layer resolution of 3-4 km, we choose a cutoff frequency



of  $f_c=1$  Hz, tapering the spectrum band-edge to suppress Gibbs-effect oscillation in the inverse FFT.

When an anisotropic layer exists, Ps conversions occur at the bounding interfaces. The Ps conversions form two-lobed or four-lobed patterns with back-azimuth. The number of lobes defines the number of polarity reversals in the RFs, e.g., two-lobed means two nearly identical lobes by backazimuth. Two-lobed components are often associated with dipping interfaces or anisotropic structures with tilting symmetry axes. One method to distinguish between a dipping interface and anisotropy is whether the direct P arrivals (zero delay time) on the transverse component are present or not. In the presence of a dipping interface, the incoming P wave is refracted out of the propagation plane as it encounters the dipping interface from any direction other than plunge-parallel. This refraction gives rise to the SH energy at zero delay time on the transverse RF component. With only anisotropy, however, out-of-plane refraction of the P wave is minimal, producing scant SH amplitude at zero delay time. An anisotropic layer with a horizontal symmetry axis (Levin and Park, 1997a; Maupin and Park, 2007) generates four-lobed Ps converted-wave amplitude variation.

To plot the back-azimuthal variation, we grouped the RFs into  $5^\circ$  back-azimuth bins so that each trace averages RF signals within a  $10^\circ$  range of back-azimuth. For waves within a small range of back-azimuth, Ps delay times from a planar interface depend on the ray parameter. This dependence gives rise to a distance-moveout effect. To investigate the epicentral distance dependence, Figure 2 shows RFs calculated for events with back-azimuths between  $110^\circ$  and  $135^\circ$  and summed into  $5^\circ$  epicentral distance bins.

### 2.2.2 Harmonic decomposition analysis

Bianchi et al. (2010) applied harmonic decomposition to each station's receiver functions to reveal the isotropic and anisotropic features of the seismic-velocity profile. The harmonic

expansion distinguishes two-lobed and four-lobed back-azimuth dependence. Decomposed RF-harmonics are computed by performing linear regression of radial and transverse RFs. In the model space, we assume that the back-azimuth variation of the amplitudes of an ensemble of RFs at each time step can be modeled as a scaled sum of  $\cos(k\phi)$  and  $\sin(k\phi)$ , in which  $k$  denotes the harmonic order ( $k=0, 1, 2$ ) and  $\phi$  denotes the back-azimuth.  $k=0$  denotes constant RF-amplitude for all back-azimuths in the ensemble. In the case of  $k=1$  and  $k=2$ , RF back-azimuth patterns show a periodicity of  $2\pi$  (two-lobed) and  $\pi$  (four-lobed), respectively. In addition, it has been shown that radial and transverse Ps amplitudes at the same delay time vary over back-azimuth with a phase shift of  $\pi/(2k)$  (Shiomi and Park, 2008). Then the coefficients for  $\cos(k\phi)$  and  $\sin(k\phi)$  ( $A(t), B(t), C(t), D(t), E(t)$ ) are calculated in the following linear system (Bianchi et al., 2010),

$$\begin{pmatrix} R_1(t) \\ R_2(t) \\ \dots \\ R_n(t) \\ T_1(t) \\ T_2(t) \\ \dots \\ T_n(t) \end{pmatrix} = \begin{pmatrix} 1 & \cos(\phi_1) & \sin(\phi_1) & \cos(2\phi_1) & \sin(2\phi_1) \\ 1 & \cos(\phi_2) & \sin(\phi_2) & \cos(2\phi_2) & \sin(2\phi_2) \\ \dots & \dots & \dots & \dots & \dots \\ 1 & \cos(\phi_n) & \sin(\phi_n) & \cos(2\phi_n) & \sin(2\phi_n) \\ 0 & \cos(\phi_1 + \pi/2) & \sin(\phi_1 + \pi/2) & \cos(2(\phi_1 + \pi/4)) & \sin(2(\phi_1 + \pi/4)) \\ 0 & \cos(\phi_2 + \pi/2) & \sin(\phi_2 + \pi/2) & \cos(2(\phi_2 + \pi/4)) & \sin(2(\phi_2 + \pi/4)) \\ \dots & \dots & \dots & \dots & \dots \\ 0 & \cos(\phi_n + \pi/2) & \sin(\phi_n + \pi/2) & \cos(2(\phi_n + \pi/4)) & \sin(2(\phi_n + \pi/4)) \end{pmatrix} \begin{pmatrix} A(t) \\ B(t) \\ C(t) \\ D(t) \\ E(t) \end{pmatrix}$$

where  $R_i(t)$  and  $T_i(t)$  are radial and transverse RFs with back-azimuth  $\phi_i$  at each time step  $t$ , respectively, and  $n$  is the number of seismic events. Next, for each harmonic order  $k$ , radial and transverse RFs are stacked with a phase shift of  $+\pi/(2k)$  in back-azimuth to enhance the features of dipping interfaces and/or anisotropy, which is referred as the “dip/anisotropy” part of the decomposed harmonic stacks. In the “dip/anisotropy” part, five time series are displayed (Fig. 3b): (1) the top one (“const”) is the constant component in the back-azimuth dependence of RFs, which is a simple stack of the radial RFs; (2) the next two traces (marked as “ $\cos(\phi)$ ” and “ $\sin(\phi)$ ”) correspond to  $k=1$ , which shows the seismic energy caused by two-lobed anisotropy or dipping interfaces; (3) the bottom two traces (marked as “ $\cos(2\phi)$ ” and “ $\sin(2\phi)$ ”) are four-

lobed expansion terms ( $k = 2$ ), which represent horizontal-axis anisotropy. These RF harmonic stacks show the distribution of SH energy due to dipping interfaces and/or anisotropy at depth. Furthermore, stacking the radial and transverse RFs with a negative phase shift of  $-\pi/(2k)$  produces the “unmodelled” part, in which the effects of dipping structures or anisotropy are suppressed. Perfectly flat-layered structure would yield no signals on the “unmodelled” part. Signals on “unmodelled” stacks violate the flat-layered assumption, suggesting a dipping interface or a reverberation with mismatched moveout, point-scattering or excessive noise. We estimate the uncertainty of RF harmonics via bootstrap resampling the data set for 50 realizations, and plotted in light green color surrounding each trace. In this study, we rotate seismic records to L-Q-T system to enhance the converted phases, in which L aligns with P-wave propagation, Q is perpendicular to L in the source-receiver plane, and T is the normal of source-receiver plane. The moveout is corrected by using the reference ray parameter profile of the IASPEI91 model.

### 2.2.3 Forward modeling

Geophysical interpretation depends on the geometry and magnitude of seismic anisotropy, which can be explored by forward modeling. Inversions for crustal anisotropy and/or dipping structure have been successfully carried out using RF waveform data (Levin and Park, 1997a; Park et al., 2004; Ozacar and Zandt, 2004; Sherrington et al., 2004; Wirth and Long, 2014). In this study, we invert for anisotropic parameters by fitting the targeted signal pattern of harmonic stacks. The advantage is that the expansion components yield information on the geometry of symmetry axis, that is, the orientation that satisfies the combination of two-lobed and four-lobed signals.

We use the ANIREC algorithm to compute three-component synthetic seismograms for a 1-D anisotropic flat-layered model (Levin and Park, 1997b). We augment an isotropic velocity model by adding anisotropic parameters, including the strike ( $\theta$ ) and plunge ( $\delta$ ) of symmetry axes, and the magnitudes of P and S anisotropy. For simplicity, we assume ellipsoidal phase velocity

surfaces for anisotropic layers, neglecting the parameter  $C$  ( $\cos(4\phi)$ ,  $\sin(4\phi)$ ). Interface depth can be estimated from the timing of signals. The symmetry-axis plunge ( $\delta$ ) can be constrained by relative amplitude of two-lobed and four-lobed Ps amplitude dependence. A horizontal axis will lead to signals only on the four-lobed terms. Synthetic tests also show that  $\delta$  and its supplementary angle yield identical signals. The strike ( $\theta$ ) can be inferred by the signal pattern, i.e. signal polarities and energy partitioning between the  $\sin(k\phi)$  and  $\cos(k\phi)$  terms. For a single anisotropic layer,  $\theta$  relates to the particle motion, which can be calculated from the amplitudes of pulses. Percent-anisotropy is scaled to fit the Ps amplitudes. A negative percentage means that the unique axis is slow axis, and vice versa. For simplicity, we set P and S anisotropy to be equal in modeling tests.

With a starting model, we compute synthetic harmonic stacks with moveout correction to compare with the RFs from data. By “trial and error”, we first fit the pronounced two-lobed and four-lobed pulses by varying anisotropic parameters. The anisotropic parameters and timing (depth) are the most robust constraints in the fitting procedure. Unfortunately, model-discrimination worsens in the deep lower crust due to the crustal reverberations in the synthetics. In the next section, we show data that indicate that Ps reverberations in this part of Tibet are rare. Next, we adjust the seismic velocities of each layer to fit the “constant” term. We fix the  $V_p/V_s$  ratio of the crust to be 1.80 (Poisson’s ratio =  $\sim 0.277$ ). This value is consistent with the observation of high  $V_p/V_s$  ratio in northeastern Tibet (e.g. Vergne et al., 2002; Yue et al., 2012). In this way, a gross model that satisfies the prominent features of RF waveforms and harmonic stacks can be found for the structure beneath the station. We evaluate goodness-of-fit from cross-correlation coefficients between synthetic and real time-domain RF. Numerous synthetic tests are required to construct one model, so an automatic inversion technique may be preferred over forward-modeling when a large number of stations are involved.

### 3. Results

#### 3.1 Receiver-function harmonic stacks

We compute multi-taper receiver functions for each station to detect the subsurface features. At all stations, Ps conversions at the Moho discontinuity are clearly identified at delay times 8-10 s on the radial RF. The large delay time corresponds to a crust of 70-90 km thick beneath the plateau, assuming a  $V_p/V_s$  ratio of 1.80. For most stations, strong signals appear after the direct P arrivals, implying complex intra-crust structures. We have also detected strong P-SH converted energy on transverse RFs (T-RFs) from 0 to 7 seconds. We interpret these signals with the presence of azimuthal anisotropy and/or dipping interfaces within the crust. As limited energy is seen at zero delay time on T-RFs for a majority of the stations, we conclude that anisotropy, not dipping interfaces, is the main cause of the SH energy. T-RF waveforms exhibit polarity switches by back-azimuth, which are associated with a two-lobed or four-lobed feature. Moreover, it is important to examine whether the signals at mid-to-lower crustal levels are caused by P-to-S conversions at the interfaces or reverberations from shallower layers. To do this, we plot RFs as a function of epicentral distance to look at the moveout effect. We find no indication that Ps conversions with deep-crust delay times are reverberated phases – see section 3.1.1 below.

Harmonic RF decomposition for most stations reveals that the “unmodelled” component shows weak signals relative to the “anisotropy/dip” component, suggesting minor deviations from flat-layered structure beneath the receivers. (Stations X4C02, X4C09, X4C10, X4D13, and X4D25 offer exceptions to this behavior.) Ps converted-phases from dipping interfaces typically lead to significant amplitude in the “unmodelled” harmonic components, due to uncompensated moveout effects. Therefore, we interpret the prominent signals on the “anisotropy/dip” stacks mainly to the presence of anisotropy. Anisotropy in the upper crust and mid-to-lower crust are evident from the high-amplitude pulses observed at 0-2 s and 2-7 s, respectively. In the upper crust, two-lobed

back-azimuth harmonics are dominant, suggesting tilted symmetry axes or dipping interfaces. At mid-to-lower crustal levels, a large portion of energy is partitioned into four-lobed harmonics, indicating horizontal or sub-horizontal symmetry axes. In contrast, the two-lobed and/or four-lobed RF patterns are weak near the Moho (8-10 s), except for stations X4C02, CBNAQ, X4D14, X4D26, and X4F04. Synthetic tests suggest that the arrival time of peak-amplitude Moho-converted Ps phases has a harmonic variation with back-azimuth when crustal anisotropy exists, see Liu and Niu (2012). This phenomenon leads to a harmonic variation of phase amplitude over back-azimuth at a fixed arrival time, which gives rise to signals on harmonic expansion terms. Consequently, observed transverse RF signals at Moho time-delays may not guarantee the presence of anisotropy at the base of crust. We illustrate this behavior below for stations X4F13, X4F15 and X4D19.

### 3.1.1 Station X4F13

Station X4F13 ( $95.91^\circ$ ,  $31.24^\circ$ ) is located to the north of the Eastern syntaxis in eastern Qiangtang terrane (Fig.1). A total of 172 RFs are obtained for X4F13, and 44 bin-summed traces are plotted as a function of back-azimuth in Figure 3a. On the radial RFs, the Moho can be identified from Ps converted phases at delay time  $\sim 9.5$  s. Clear Ps converted phases (color-shaded) prior to Moho Ps imply that the crust consists of multiple layers with sharp interfaces. Signals on the transverse RFs indicate seismic anisotropy. At 0-2 s, RF signals appear on both R and T components. Their conjoined behavior suggests that an anisotropic layer lies within the upper crust. Two columns of high-amplitude pulses (yellow-shaded) appear at  $\sim 2.5$  s and  $\sim 3.5$  s, corresponding to the two boundaries of the layer. A notable polarity change (black star) occurs at  $\phi = \sim 60^\circ$  in the radial RFs and at  $\phi = \sim 105^\circ$  in the transverse RFs. This is strong evidence of azimuthal anisotropy in the middle crust. A phase shift of  $\sim 45^\circ$  between radial and transverse component corresponds to four-lobed anisotropy. This result can be explained with an anisotropic

layer with a horizontal or sub-horizontal symmetry axis. Another series of strong pulses (green-shaded) appear later at 4.5-7 s, which switches polarity near  $\phi = \sim 100^\circ$  on the transverse RFs.

On the “constant” back-azimuth harmonic for station X4F13 (Figure 3b), the high-amplitude positive pulse at  $\sim 1$  s delay could be due to a large velocity jump near the surface. The negative pulse at  $\sim 2.5$  s could be associated with a crustal low-velocity layer. Positive pulses at  $\sim 3$  s and  $\sim 6$  s indicate sharp interfaces in the mid-to-lower crust. Another big positive pulse at  $\sim 9.5$  s marks the Moho discontinuity. Next, we examine the two-lobed and four-lobed terms as indicators of azimuthal anisotropy. Both two-lobed and four-lobed signals are generated at shallow depths (0-2 s), suggesting a symmetry axis that tilts between the vertical and horizontal orientations. Between 2 and 4 s, a pair of negative and positive RF harmonics are evident on the  $\cos(2\phi)$  and  $\sin(2\phi)$  terms. These are equivalent representation of the strong four-lobed pattern in Fig. 3a. Energy on two-lobed terms is relatively small, suggesting an anisotropic layer with a near horizontal symmetry axis. Strong signals at 4.2-7.0 s exhibit similar patterns to 2-4 s, indicating a deeper anisotropic layer with similar symmetry orientation.

At Moho depth ( $\sim 9.5$  s), both two-lobed and four-lobed RF harmonics are relatively weak. However, the delay times of Pms phases (Ps phases converted at Moho) exhibit a harmonic variation on the radial component (Fig. 3a), which could be caused by azimuthal anisotropy within the crust. This observation agrees well with previous RF data and synthetic results (Sun et al., 2012; Liu and Niu, 2012). This harmonic feature also creates a harmonic variation of the peak Ps amplitude over back-azimuth at a certain delay time. Therefore, signals at  $\sim 9.5$  s may not be robust evidence of anisotropy at the deep crustal interface. Instead, we suggest that anisotropy at the base of crust could be very weak. On the “unmodelled” component, limited energy is evident, except the big signal at  $\sim 5$ -s delay on the  $\cos(\phi)$  RF harmonic. This “unmodelled” harmonic term could be caused by the presence of complex heterogeneities that generate unusual Ps scattering.

The epicentral distance dependence of X4F13 RFs is demonstrated in figure 4a. Principal upgoing P-to-S converted phases show negative or no moveout as epicentral distance increases, but multiple reflections display a positive moveout with epicentral distance. In Fig. 4a, consistent Moho phases (green line) are observed at ~9-10 s. Positive pulses at ~6 s (purple line) display no moveout, indicating a Ps conversion at a lower-crustal interface. A series of high-amplitude negative pulses at 3-4 s (black curve) show a positive moveout. However, a synthetic test (Fig. 4b), in which primary conversion occurs at ~0.8 s (orange line), suggests that the negative reverberation signals at 3-4 s (solid black line) should be accompanied by equally strong positive reverberated phases at 2-2.5 s (dashed black line), which is not observed in the real data (Fig. 4a). In addition, the observed positive moveout in Fig. 4a is much larger than the predicted moveout in Fig. 4b. The positive moveout at 3-4 s is not likely an indicator of multiple reverberations, but may be caused by direct Ps scattering from a nonplanar structure beneath the station. Moreover, reverberations from shallow interfaces only introduce stronger late-arriving signals to the radial component, but transverse RF-signals with large delay-times should not be contaminated. The prominent signals after ~3 s on the transverse component (Fig. S3a) also argue for primary Ps conversions in deep crust.

### 3.1.2 Station X4F15

Station X4F15 (93.78°, 31.87°) is located north of Bangong-Nujiang Suture (BNS) (Fig. 1). Moho Ps is seen from positive pulses at ~8.5 s on the constant ( $k=0$ ) radial RF (Fig 5a). Back-azimuth RF dependence shows converted Ps conversions with polarity change on both R and T receiver functions. At 1-2 s, the pulse polarity-switch at  $\phi \sim 180^\circ$  on T-RFs indicates two-lobed anisotropy. From 2 to 4 s (yellow-shaded), the polarity flips at  $\phi = \sim 90^\circ$  and  $\phi \sim 135^\circ$  on R and T component, respectively. This pattern suggests the four-lobed RF harmonic in the middle crust. In addition, at 5-6.5 s (green-shaded) polarity switch occurs at  $\phi \sim 135^\circ$  on R-RF and  $\phi \sim 90^\circ$  on T-RF. This four-lobed behavior is strong evidence of an anisotropic lower-crustal layer with near-



horizontal symmetry axis. Some energy shows up at 7.5-8.5 s on T-RFs, but may not be as persuasive an indicator of anisotropy beneath X4F15. Below the Moho (~10-11 s), we also note the positive signals between  $\phi = \sim 120^\circ$  and  $\sim 180^\circ$  on the radial component and the negative pulses between  $\phi = \sim 30^\circ$  and  $\sim 120^\circ$  on the transverse component, which may suggest a surface of localized-shear, but not a compositional jump, in the uppermost lithospheric mantle.

Figure 5b shows the result of harmonic analysis of X4F15 RF data. On the “anisotropy/dip” RF harmonics, five traces all exhibit high-amplitude signals. On the “constant” term, the blue pulse at ~1 s indicates near-surface velocity jump. The big negative pulse at ~5.5 s may be associated with a low-velocity layer. Moho is revealed by the high-amplitude positive pulse at ~8.5 s. Moreover, notable pulses are present on  $\cos(\phi)$  and  $\cos(2\phi)$  terms at 1-2 s, indicating anisotropy with a tilting symmetry axis. From ~2.5 s to ~3.5 s, major energy occurs on  $\cos(2\phi)$  and  $\sin(2\phi)$  terms. On the  $\sin(2\phi)$  term, a positive pulse is seen at ~2.5 s, followed by a negative pulse at ~3.5 s. The paired pulses correspond to two boundaries of one anisotropic layer. On the  $\cos(\phi)$  term, however, there is only one big pulse from ~2 s to ~4 s. From ~3.5 s to ~5 s, a positive and negative pulse appear on the  $\sin(\phi)$  term, defining another anisotropic layer. The pair of huge signals from ~2 s to ~5 s on the  $\cos(2\phi)$  term could be an overlap of scattered waves from two juxtaposed anisotropic layers with similar symmetry directions. Another anisotropic layer is revealed from two pulses between 6 s and 7.5 s on  $\cos(2\phi)$  term. Energy on the “unmodelled” part is very weak compared to the prominent signals on “anisotropy/dip” part, implying a flat-layered structure beneath the station.

### 3.1.3 Station X4D19

X4D19 (94.92°, 34.27°) is located in the northern part of the study area (Fig. 1). RFs are obtained and plotted against back-azimuth in figure 6a. We identify Moho discontinuity at 9-10 s on R-RFs. Major anisotropic features are evident from large SH energy at 2-7 s on T-RFs. Polarity change

occurs on T-RFs near  $\phi=140^\circ$  at 2-4 s (yellow-shaded) and near  $\phi=120^\circ$  at 5-6.5 s (green-shaded). On the R-RFs, however, it is not as clear as in previous examples. More information needs to be extracted by decomposing RFs into harmonic expansion terms (Fig. 6b). On the “constant” term of the “anisotropy/dip” part, the blue pulse at 0.5 s indicates a velocity increase in the uppermost crust. The red pulse at  $\sim 3$  s may be associated with a low-velocity layer in the middle crust. The positive pulse at 9-9.5 s shows the depth of Moho. On the  $\cos(\phi)$  term, the positive pulse at  $\sim 1$  s implies two-lobed anisotropy which could be caused by aligned faults near the surface. Positive and negative signals at 3-4 s on the  $\sin(\phi)$  and  $\cos(2\phi)$  harmonics may be caused by an anisotropic layer in the middle crust with a tilted symmetry axis. But on the  $\sin(2\phi)$  RF harmonic, the Ps pulses are fatter and expand from 2-4 s. At 5-6.5 s, similar pattern (a positive pulse followed by a negative pulse) appears on the  $\sin(\phi)$ ,  $\cos(2\phi)$  and  $\sin(2\phi)$  RF harmonics. The result of harmonic analysis suggests that there might be two anisotropic zones (2-4 s and 5-6.5 s) in the middle and lower crust. At Moho depth, however, only weak evidence of anisotropy is apparent.

### 3.2 Forward modeling

Based on the RF stacks, a majority of stations display common features: evidence for localized anisotropy appears at mid-to-lower crustal levels. To investigate their implications on the seismic structures, we forward-modelled RF estimates from stations X4F13, X4F15, X4D19, X4B02 and X4D10. For all but one station, we choose a slow axis due to the crustal preference for aligned sheet-silicate minerals and fine-layering effects (Okaya and Christensen, 2002). For station X4D10, no solution in parameter space could be found for slow-axis symmetry to reconcile the two-lobed pattern and four-lobed pattern. We used fast-axis symmetry for this station to obtain good fit. Our inversion results have successfully constrained the depth and geometry of observed anisotropy in RFs and harmonic stacks. We first evaluate the fit by careful visual comparison of synthetics and real data. For a more quantified estimation, we compute the cross-correlation. We are able to fit the major phases well with least complexity. Minor discrepancies still remain between the synthetics and real data, perhaps due to lateral heterogeneity.

All preferred models include anisotropic zones located in the upper, middle and lower crust. These anisotropic zones are separated by isotropic layers. Radial anisotropy does not convert P to SH polarized motion, and does not lead to 2-lobed or 4-lobed back-azimuth variation in Ps amplitude. Therefore, the layers that we model as isotropic could contain radial anisotropy, as suggested by surface-wave studies (Duret et al., 2010; Xie et al., 2013). Upper-crust anisotropic layers mainly contain tilted axes ( $\delta=45^{\circ}$ - $70^{\circ}$ ), with thicknesses of 4-6 km. For the middle- and lower-crust anisotropic zones, layer thicknesses and percent-anisotropy vary from model to model. But a common feature is that they mostly contain horizontal to sub-horizontal axes ( $\delta=75^{\circ}$ - $90^{\circ}$ ). Furthermore, in most models (except X4D10), similar strike directions are inverted for the two anisotropic zones in middle and lower crust. Although there may be other solutions due to the non-uniqueness of forward modeling, our preferred models convey a consistent picture of deformation across the region.

The radial local maxima computed from the two-lobed and four-lobed RF stacks (see the supplement for details) show that most stations consistently display NE-SW symmetry directions in middle crust (a delay time of  $\sim 2$ -4 s). However, local variation in symmetry-axis orientation is also recognized. The inferred orientation of anisotropy at each of the selected stations is not necessarily representative of surrounding stations, though we note correlations between stations (Fig. S6). Orientation of the axis of anisotropy can be variable by virtue of local deformation processes (Nikulin et al., 2009). Here we will illustrate the results of station X4F13, X4F15 and X4D19.

### 3.2.1 Station X4F13

We construct an anisotropic velocity model based on the harmonic expansion terms of estimated receiver functions (Fig. 7). These harmonic stacks capture the most striking features of the real data (Fig. 8). Only the “Dip/Anisotropy” part is compared because the synthetic “unmodelled” stack has negligible amplitude. A large  $V_p$  jump from 5 km/s to 6.2 km/s at the 4.1-km interface leads to the blue pulse at  $\sim 1$  s on the “constant” trace. The anisotropic layer from 4.1 km to 10 km consists of a tilted slow axis ( $\delta=70^\circ$ ) at near NNE-SSW strike ( $\theta=15^\circ$ ). It gives rise to the signals between 0 s and 2 s. 10% anisotropy is needed to fit the signal amplitudes. With a tilt angle of  $70^\circ$ , two-lobed harmonics of back-azimuth variation are dominant relative to the four-lobed RF harmonics. A strike of  $15^\circ$  is chosen such that major two-lobed  $P_s$  amplitude occurs on the  $\cos(\phi)$  term and four-lobed energy splits to the  $\cos(2\phi)$  and  $\sin(2\phi)$  term. At the 23.2-km middle-crust interface, the velocity drop of  $\sim 2\%$  contributes to the negative pulse at  $\sim 2.5$  s on the constant term. Between 23.2-27.8 km, 15% four-lobed anisotropy with  $\delta=90^\circ$  and  $\theta=15^\circ$  in a low-velocity zone successfully fits the anisotropic signals at 2-4 s. No two-lobed signal is created because we model the anisotropy with a horizontal symmetry axis. The slow axis at  $\theta=15^\circ$  strike generates a negative signal at  $\sim 2.5$  s and a positive signal at  $\sim 3.5$  s on both  $\cos(2\phi)$  and  $\sin(2\phi)$  terms. The  $\cos(2\phi)$  harmonics have slightly higher amplitudes than  $\sin(2\phi)$ .

In the lower crust, an anisotropic layer from 45 km to 60 km with the same symmetry orientation generates the four-lobed signals between 5 s and 7 s. Average  $V_p$  increases from 6.4 km/s to 7 km/s across the 60-km-interface, corresponding to the positive signal at  $\sim 7$  s on the constant term. One notable feature is that four-lobed signals at  $\sim 9.5$  s are well fit although the model does not include an anisotropic layer at the bottom of crust. It implies that the lowermost crust could be rather azimuthally isotropic. Furthermore, we calculate the cross-correlation coefficients to estimate the quality of fitting to the original data (Fig. 8). Since we did not attempt to fit the low-amplitude pulses on the  $\sin(\phi)$  term, it shows a very low cross-correlation (-0.09). Although the cross-correlations of the other four terms are not very close to 1, values of 0.51-0.77 still indicate a high degree of correlation because we only target the most prominent signals for fitting. In addition, major features of RF waveforms are also reproduced well by this model (Fig. S4a). Targeted polarity changes occur at the same back-azimuth and delay time as in real RFs (Fig. 3a) on R and T component.

### 3.2.2 Station X4F15

Our preferred X4F15 model includes an anisotropic layer at 6-12 km in the upper crust (Fig. 9). A slow axis with  $\delta=60^\circ$  and  $\theta=180^\circ$  produces anisotropic signals on  $\cos(\phi)$  and  $\cos(2\phi)$  at 1-2 s (Fig. 10). The middle-crust anisotropic zone consists of two consecutive anisotropic layers. This double-layer structure is required to reproduce the signals from  $\sim 2$  s to  $\sim 5$  s. Although it is a complex structure, symmetry orientation of these two layers are similar. The first layer (22-32 km) of the middle-crust anisotropic zone has 12% anisotropy with a horizontal slow axis pointing to  $\theta=105^\circ$ . It generates a pair of positive and negative signals on  $\cos(2\phi)$  and  $\sin(2\phi)$  at 2-4 s. The layer beneath (32-40 km) contains 13% anisotropy with a sub-horizontal slow axis orienting E-W. It gives rise to the pulses at 3-5 s on the  $\sin(\phi)$  and  $\cos(2\phi)$  term. As its strike is  $90^\circ$ , there is no signal on the  $\sin(2\phi)$  term. These two layers each produce a positive and a negative signal on the  $\cos(2\phi)$  term. As a consequence, the broad signal the model generates at 2-5 s on  $\cos(2\phi)$  term is

a composite of the two pairs of signals. Despite the slight difference in anisotropic orientation between the two layers, they together comprise a thick anisotropic zone (18 km) in the middle crust. At the 40 km interface, a velocity decrease is necessary to suppress the positive signal at ~5 s on the “constant” trace.

In the lower crust, another anisotropic layer from 55 km to 62 km contributes to the pulses on  $\cos(2\phi)$  at 6-7 s. At the 62-km interface,  $V_p$  jumps from 6.55 km/s to 7 km/s, causing the little positive signal at ~7.2 s on the constant term. Cross-correlation values confirm that our model provides a good fit to the data (Fig. 10). Correlations are in the range of 0.44-0.84. Similar to X4F13, we also see two anisotropic zones in the middle and lower crust beneath X4F15. But in this case, two symmetry axes are consistently directed eastward. It implies that the crustal structure in this area could be complicated.

### 3.2.3 Station X4D19

X4D19 model also has anisotropy located in three crustal zones (Fig. 11). As shown in Figure 11, the top 4 km of the crust has relatively weak anisotropy (5%). The slow axis has a tilt  $50^\circ$  from the vertical and a strike of  $210^\circ$ . It is responsible for the positive signal at ~0.5 s on  $\cos(\phi)$ . From 21 km to 36 km, there is a double-layer zone with a large amount of anisotropy (10-14%). The middle-crust layer (21-28 km) includes a horizontal slow axis orienting  $\theta=130^\circ$ . This depth and symmetry direction should generate a positive pulse preceding a negative one at 2-3 s on  $\sin(2\phi)$ . We do not see this pattern at 2-3 s because the lower anisotropic layer (28-40 km) also creates the same pattern on  $\sin(2\phi)$  at 3-4 s. Therefore the wide signal we see between 2 s and 4 s on  $\sin(2\phi)$  term is a signal overlap of two groups of signals (Fig. 12). We have encountered similar situation in the X4F15 model. The lower layer also generates arrivals on the  $\sin(\phi)$  and  $\cos(2\phi)$  term. In the lower crust, we use an anisotropic layer from 50 km to 60 km to reproduce the signals at 5-7 s in Fig. 6b. Both the middle and lower crustal layers indicate (sub-)horizontal axes in the ESE-

WNW direction. The correlation coefficients are high (0.58-0.83), aside from the  $\cos(\phi)$  term (0.34), which has low signal-to-noise ratio (Fig. 12). Thus, this model is a good candidate for the local crustal structure.

#### 4. Discussion

Receiver functions offer constraints on shallow earth structure that are complementary to those offered by regional surface waves, Pn waves, seismic attenuation, seismicity distribution and field tectonics. By combining radial and transverse RFs, we can detect and characterize sheared layers within the Tibetan crust, and relate them to possible lithologic and compositional transitions. In this section we discuss our RFs estimates in the context of popular tectonic-origin scenarios for the plateau. We suggest that, in order to fit fully the detailed back-azimuth variation of the RFs, seismologists may need to expand their interpretation toolkit beyond conventional shearing models and include the influence of metamorphic processes on crustal fabrics.

##### 4.1 Isotropic profiles of seismic velocity

Isotropic crustal velocities consistent with our receiver-functions estimates and forward modeling are broadly similar to those reported for central Tibet by Nabelek et al. (2009). Receiver functions are sensitive more to velocity jumps at interfaces than to the absolute velocity, so we anchor our models by taking the underlying mantle as an isotropic half-space with a  $V_p$  of 8 km/s based on the local Pn wave velocity reported by Lei et al. (2014), and consistent with peridotite lithology. Velocities of each crustal layer are estimated by fitting the Ps amplitudes with velocity increment or decrement from the layer beneath. We fix  $V_p/V_s=1.80$  through the crust, which is intermediate between mafic and felsic properties. At the base of the crust, a high velocity layer ( $V_p$  near 7 km/s) is required for models with high “constant-term” correlation coefficient ( $>0.6$ ), consistent with the seismic properties of mafic granulite and mafic amphibole facies rocks (Christensen and Fountain, 1975; Rudnick and Fountain, 1995). In contrast,  $V_p$  of the layers lying above is found to be in the range of 6.2-6.55 km/s, typical of felsic granulite or felsic and pelitic amphibolite facies rocks (Rudnick and Fountain, 1995). At the top of the crust,  $V_p$  is found to be as low as 5 km/s, probably due to the sedimentary rocks or crystalline rocks that are fractured. Greater



uncertainty in  $V_p$  can be assumed for shallow layers in our modeling, because we have fixed the  $V_p/V_s$  ratio to lie above values appropriate for felsic igneous and sedimentary rocks.

In the middle crust, a low-velocity layer at ~20-30 km is detected for two stations (Fig. 7 and 11), consistent with the high electrical conductivity (Bai et al., 2010) and widespread LVZs constrained by other seismological studies (e.g. Nelson et al., 1996; Yang et al., 2012). Low seismic velocities have been interpreted to be associated with high-temperature conditions. In continental crust, volatile release or partial melting could occur at high temperatures due to metamorphic alteration of hydrous minerals (Patiño Douce and McCarthy, 1998; Skjerlie and Patiño Douce, 2002). The presence of partial melt or fluid  $H_2O$  could explain sufficiently the low seismic velocities (Williams and Garnero, 1996). Also, migration of hydrothermal fluids through veins could precipitate less-rigid minerals such as quartz (e.g. Breeding and Ague, 2002). Olugboji et al (2013) argue that low-velocity steps in receiver functions at the base of the mantle lithosphere are caused by a rheological effect called grain-boundary sliding (Lee and Morris, 2010; Karato, 2012) that is well-known in metals (Kê, 1947) and is analogous to the effects of pre-melting in glacier ice (Wettlaufer, 1999; Dash et al, 2006). Grain-boundary sliding should occur in crustal rocks as well as in peridotites, and therefore is another possible cause of mid-crustal inversions of seismic velocity.

However, an LVZ is not suggested in all RF profiles, some of which are fit adequately by  $V_p$  in the 6.1-6.5-km/sec range, monotonically increasing with depth. The absence of LVZs in our preferred models is possibly caused by the trade-off of anisotropic effects and isotropic RFs in synthetic RFs, because we focus on fitting the azimuthal RF variations in our trial-and-error modelling. In the crust, the absence of partial melt could be caused by a lowered activity of water associated with a mixed  $H_2O$ - $CO_2$  fluid (e.g. Valley et al., 1990). Strong layering of chemical composition and volatile content in the Tibetan crust could fix the grain-boundary-sliding

transition at a lithologic boundary; a downward transition from a less-rigid to a more-rigid rock type could compensate the effect of grain-boundary relaxation.

If Tibet formed by the wholesale underthrusting of Indian crust beneath Eurasian crust, one might expect India-derived surface rocks to lie, like cheese in a sandwich, in the middle crust. Consequently, the presence of upper-crustal rocks in the mid-crust would appear as a low-velocity zone near the middle of the RF profile. However, our isotropic RF profiles do not provide widespread evidence for this. Although located within anisotropic shear zones (see below), thin low-velocity mid-crustal layers are suggested only beneath a minority of stations. Similarly, a Eurasian-crust companion to the high-velocity layer ( $V_p > 7$  km/s) at the base of the RF crustal profiles is not observed in the middle crust at any station we modeled. Most of the isotropic RF crustal profiles suggest a downward-increasing  $V_p$  through (up to) 80 km of crustal rocks in a single petrologically mature profile. Increasing wavespeed is consistent with the shortening/thickening model for Tibet, but we suggest below that the crustal profile beneath our stations is a product of metamorphism, and perhaps magmatism, during collision, rather than passive thickening of a pre-existing crustal profile.

#### 4.2 Constraints from azimuthal anisotropy

We estimated back-azimuth harmonic expansions of receiver functions for 35 stations within the ASCENT experiment, and developed 1-D anisotropic seismic profiles for 5 of the stations via forward-modeling with synthetic seismograms with a reflectivity code. The RFs for the chosen 5 stations are similar to the RFs obtained from the other stations, so we believe that the broad features of the 1-D seismic profiles are characteristic of the crust in the ASCENT field area of northeastern Tibet. We infer anisotropic layers located, roughly speaking, at three different depths. Our anisotropy profiles are not uniquely determined by the receiver functions, but are constrained by prior assumptions that we believe to be reasonable. First, in most cases we specify anisotropy

to possess a slow symmetry-axis in crustal rocks, consistent with the lattice-preferred orientation (LPO) of sheet silicates and shape-preferred orientation (SPO) of rock textures that are layered on length scales more fine than seismic wavelengths ( $\lambda > 5$  km). Second, we seek anisotropy profiles that contribute weakly to SKS splitting, because typical estimates of shear-wave birefringence suggest delay times of 0.5 s or less (Liu and Niu, 2012). Large anisotropies at interfaces are required to model the Ps waves that are generated within the Tibetan crust, but most Ps conversions are observed in pairs of opposing polarity, consistent with being generated by the top and bottom of relatively thin sheared layers.

With some variation in depth range among stations, as well as in anisotropic strength and orientation, we observe distinct anisotropic layers at all stations modeled. Upper-crustal anisotropy shows two-lobed Ps amplitude variation with back azimuth, which can be associated with a tilted symmetry axis (Levin and Park, 1998). In addition, strong anisotropy is concentrated in the middle-to-lower crust of the study area, consistent with previous studies (Sherrington et al., 2004; Ozacar and Zandt, 2004). However, we propose horizontal or sub-horizontal slow axes for some of the stations in contrast to radial anisotropy (e.g. Xie et al., 2013). Based on our observations, we would like to address the following questions: (1) What are possible causes of the observed azimuthal anisotropy? (2) What are the geological and geophysical implications?

Azimuthal anisotropy in the upper crust is often interpreted as caused by near-surface geologic structures such as aligned microcracks (e.g. Kaneshima 1990; Crampin and Chastin, 2003). Microcracks in the deep upper crust can be sealed and filled with fluids or mineral deposits (Crampin and Chastin, 2003). This effect and aligned-layering texture can be approximated by hexagonal symmetry with a slow axis along the plane-normal. Two-lobed anisotropy at 0.5-2 s is a good indicator of tilted-axis anisotropy consistent with a collisional thrusting texture in the near-surface geology. In the deeper crust, two other major back-azimuth-dependent Ps signals appear between delay times of 2 s and 7 s, suggesting strong anisotropy in the mid-to-lower crust.

These signals can be fit by two distinct anisotropic layers at ~20-35 km and ~45-60 km that contain symmetry axes trending at similar directions, consistent with two shear zones above and below a flowing lower-crust layer (Clark and Royden, 2000). Anisotropy in the deep crust could be caused by the LPO of mineral grains. The best candidates for preferential alignment are hydrated silicate minerals that are polymerized into sheets or needles, such as micas and amphiboles. Mica develops a strong fabric with the (001) plane parallel to foliation, with a foliation-normal slow axis. The LPO of muscovite can make significant seismic anisotropy due to its highly symmetrical structure (Barruol and Mainprice, 1993; Barruol and Kern, 1996). Amphiboles are hydrated silicate minerals that develop LPO in stained rocks, often as a result of foliation, often with a slow axis of symmetry (Ji et al., 2013). In this study, we infer as much as 10-15% anisotropy for some layers, which can be accounted for by aligned micas. Anisotropic signatures of other crustal minerals, such as amphibole, are less strong, but probably could help explain our RF behavior.

Another possible source of bulk anisotropy is shape-preferred orientation (SPO) associated with aqueous fluids or melts embedded within crustal rocks. Layered structure formed by aligned tabular fluid domains produces hexagonal symmetry with a unique slow axis (Tandon and Weng, 1984; Kendall and Silver, 1996). There has been evidence showing fluid-filled cracks in lower crustal rocks (Ague, 1994, 1995) and subducting oceanic slabs (Healy et al., 2009). Consequently, SPO of aligned fluid or melt disk-like domains should also be considered, even though the ability of fluids to persist in vertical cracks throughout 5-15-km-thick crustal layers is not well established. Therefore, in the next section we introduce other mechanisms for developing SPO within the Tibetan crust that we believe are more likely to explain the seismic anisotropy of the Tibetan crust.

#### 4.3 Geophysical implications

Concerning the Tibetan Plateau, two major crustal-thickening mechanisms have been suggested, i.e. crust underthrusting (e.g. Zhao and Morgan, 1987) and horizontal shortening (e.g. Dewey et al., 1988). Channel-flow models have been proposed for the dynamic evolution of Tibetan crust (Nelson et al., 1996; Clark and Royden, 2000; Beaumont et al., 2004; Klemperer 2006). In this section, we first evaluate LPO anisotropy from aligned hydrated-silicate minerals, such as micas and amphiboles, by examining popular geodynamic models. Shear zones have been widely used to explain observed tilted-axis anisotropy (e.g. Levin and Park, 2000). However, problems rise when we try to connect deep-crustal horizontal-axis anisotropy to shear zones. We will first chronicle the difficulties, and then hypothesize mechanisms for resolving them.

Seismological evidence that underthrusting of Indian or Eurasian crust may have occurred beneath the Tibetan crust has been reported by, e.g., Kind et al. (2002), Jackson et al. (2008) and Nabelek et al. (2009). A large-scale underthrusting process would involve shear localization near upper and lower boundary of the underthrusting crust. Shear-induced anisotropy would be strong in the middle crust and near the Moho. Pronounced anisotropic features have been found in mica-bearing mylonites sampled from various shear zones around the world (e.g. Siegesmund and Kern, 1990; Kern and Wenk, 1990; Ji and Salisbury, 1993). In simple shear, sheet-silicate minerals are rotated and aligned in response of applied shear stresses. As a result, these mylonitic rocks exhibit a slow axis perpendicular to the foliation plane. Tilted or near-vertical slow-axis anisotropy would be expected if underthrusting had taken place. In our study, however, RF results show substantial slow-axis anisotropy with near-horizontal orientation. Simple shear that bounds the mobile lower crust of Tibet will not rotate sheet silicates to align vertically, unless block-rotations of large parcels of rocks within the shear zone occur as a slow-motion nonlinear instability. We do not know of deep-crust field exposures that show such behavior, so we conclude that the underthrusting mechanism cannot explain our observation of near-horizontal slow-axes in the middle- and deep-crust shear zones.

On the other hand, the distributed shortening and thickening model also has difficulty in explaining the data. RF modeling reveals that significant anisotropy (10-15%) can be concentrated in multiple zones in the middle and lower crust. Assuming anisotropy is caused by sheet silicates or similarly hydrated mineral, pure shear within the entire crustal profile would generate a uniformly anisotropic crust, similar to the assumption made in the Ps-splitting estimates from Tibet RFs by Liu and Niu (2012). Also, a strain of  $\sim 1$ , which would thicken the crust by 100%, may not be enough to align sheet-like minerals vertically. Therefore, a simple crustal shortening model is not favored by our data.

Channel-flow models refer to crustal rocks that flow within a rheologically-weak depth range. Supporting evidence from magnetotelluric data (Wei et al., 2001; Unsworth et al., 2004; Bai et al., 2010) has imaged low electrical resistivity zones in mid-lower crust across most of Tibet. LVZs inferred from seismic tomography have also been suggested to be associated with channel flows (e.g. Yang et al., 2012). Two simple numerical models are often used to describe channelized flows, i.e. Couette flow and Poiseuille flow (pipe flow). Couette flow happens when drag force is applied at one boundary where highest velocity is produced. Shear occurs across the channel but diminishes at the other boundary. In contrast, in Poiseuille flow, strong shear often occurs near the upper and lower boundary of a flowing layer due to a large velocity gradient. In the central part (in depth) of the channel, the velocity gradient is small and materials move more coherently. In terms of seismic anisotropy, Poiseuille flow would generate a large amount of anisotropy near the two boundaries of the flow that possesses a more-isotropic interior.

An important feature of our velocity models is that a layer that lacks azimuthal anisotropy is sandwiched by two layers in the middle and lower crust that have similar horizontal symmetry-axis directions, consistent with shear zones at the boundaries of a  $\sim 30$ -40-km-thick flowing layer (Fig. 13). Although the arrangement of anisotropic layers and seismic velocities in our RF profiles suggests strongly the familiar model of lower-crust channel flow beneath the Tibetan

Plateau (Clark and Royden, 2000), details of the inferred anisotropy are difficult to explain in terms of simple kinematic flow models. Strong four-lobed Ps amplitude variations suggest horizontal slow axes, but simple shear in the boundary layers would yield a tilted, rather than a horizontal, symmetry axis. For this reason, a simple Poiseuille flow cannot convincingly explain our RFs if we assume aligned sheet silicates as the cause of anisotropy. A more sophisticated mechanism in which rotation of sheet silicates due to boundary-layer shear instability is possible but its ability to rotate pre-existing LPO to a consistently horizontal symmetry axis is unlikely.

Alternatively, horizontal-axis anisotropy can be generated by the SPO of vertical interlayering textures. A layer with vertical interlayering of different rock types analogous to the southern Adirondacks (McLelland and Selleck, 2011) could give rise to horizontal slow-axis anisotropy. SPO can also form by fluid-filled veins (Ague, 1995), ribbons of precipitated minerals (McLelland, 1984), melt inclusions, or diapirs (Kendall, 2000). High-temperature metamorphism in the deep crust may produce substantial volumes of fluid through the dehydration of hydrous minerals such as amphibole and muscovite. Upon shear stresses, tensile cracking may occur due to the fluid transfer. Tensile cracking produces fault planes at angles  $\sim 45^\circ$  to the horizontal, but near-vertical conduits may develop via the upward transport of fluids via en-echelon cracks (Rubin, 1995). Also, it has been predicted that hydrothermal fluids could transfer efficiently as porosity waves through vertically oriented chimneys in the lower crust (Connolly and Podladchikov, 2004). Therefore, we consider SPO by fluid transfer in the deep crust as a good alternative to explain the four-lobed anisotropy that we observe.

In the context of pipe flow, dehydration could take place due to shear-induced heating in the boundary layers. Released metamorphic fluids could form vertical conduits with the shearing boundary layers. In our data, low seismic velocities of the anisotropic zone in the middle crust ( $\sim 20$ -40 km) (Fig. 7 and 11) may require the presence of melts. Partial melting could be further driven by the fluids released from hydrous protoliths such as metapelites (Thompson and

Connolly, 1995; Whitney et al., 2004). Theoretical study has shown that temperature may be high enough to cause partial melting in the middle crust due to a high concentration of radiogenic elements (McKenzie and Priestley, 2008). Finally, the presence of fluids could activate subsolidus grain-boundary sliding (Olugboji et al, 2013) to produce a velocity drop.

However, low seismic velocities are not obvious in the lower-crustal anisotropic layer (lower boundary layer), implying no partial melting in lower crust. Different P-T conditions, rock types or fluid history between the middle and lower crust may all contribute to their contrasting melting behaviors. High CO<sub>2</sub> content in metamorphic fluids will lower the water activity, suppressing partial melting. It is also possible for water to be rehydrated by the layer above, leaving altered compositions in the fluid domains that form vertically-oriented layering. Therefore, horizontal-axis anisotropy might be an indicator of metamorphic events within or near the shearing boundary layers. In this case, the anisotropic structure in mid-to-lower crust (~20-60 km) predicted by our models can be explained by metamorphism that, in part, lubricates the channel flow.

Below the major deep-crust shear zones, we infer a mafic, weakly anisotropic layer at the base of northeastern Tibetan crust. Nabelek et al (2009) identify in migrated receiver-function images a basal eclogite layer in underthrusting Indian crust in Hi-Climb data. The Ps converted phase used to delineate the Vp~7 km/s “eclogite” layer cannot be followed into the converging Indian plate, and the penetration of this layer halts at 31°N, south of the stations we analyze. Alternatively, mafic composition in the lowermost crust could have been emplaced by gabbroic melts from the rising asthenosphere in a delamination event (Fountain, 1989; Dong et al., 2005; Xu et al., 2013). Fountain (1989) argues that magmatic underplating should crystallize into mafic granulites. At these depths a conversion from gabbro to eclogite would likely destabilize the crust (Krystopowicz and Currie, 2013; O’Rourke and Korenaga, 2012), but a less-dense mafic granulite would be less likely to delaminate. A strong mafic/eclogitic basal layer may be required to maintain the Tibetan plateau during the retreat of the Eurasian slab (Gray and Pysklywec,



2012). The mafic basal layer may have undergone dehydration and become rheologically strong. Lack of robust anisotropy in this layer in our crustal models would be consistent with a strong rheology.

If the protolith of the Tibetan crust were petrologically-mature continental crust from Eurasia and India, the release of widespread volatiles in the deep crust of the plateau, as we have interpreted from our RF modeling, would be puzzling. Originally lying within the high-grade metamorphic zones, a protolith lower continental crust contributed by the colliding plates should arrive dry. An alternative protolith was suggested by Yakolev and Clark (2014). They compute past and present crustal volumes for the Tibetan plateau, and conclude that 30% of a mature continental-crust protolith would now be missing. Yakolev and Clark (2014) suggest that thin continental crust (23-29 km), topped by a marginal sea similar to the present-day Mediterranean, was trapped between the colliding plates. Elsewhere in the closure of the Tethys Ocean, inland seas have been trapped and deformed in orogenic events, contributing substantial volumes of metacarbonates and metapelites to the crystalline-basement rocks, e.g., in the Italian Apennines (Festa et al., 2010).

Orville (1969) proposed a metamorphic pathway for interbedded carbonates and pelites to release both  $H_2O$  and  $CO_2$  and to transform into high-grade amphibolite rocks. This process could even form mafic rocks if dolomites were part of the mix. Ague (2003) reports extensive calc-silicate rocks in the Wepawaug Schist of northeast USA, which are consistent with the scenario suggested by Orville (1969). One intriguing consequence of the Orville (1969) model is that the contribution of  $CO_2$  to the transport of metamorphic volatiles would suppress the activity of  $H_2O$  and suppress partial melting (e.g., Valley et al., 1990), allowing the Tibetan collision to appear today to have resulted from structural/tectonic processes, rather than metamorphic/igneous processes. If Orville's metamorphic scenario correctly applies, then sediment-covered thin continental crust, lying beneath the Tethyan marginal seas, transformed into the deep crust of

Tibet. This scenario represents a third formation-story for Tibet, a metamorphic brother to the structural shortening and underthrusting models.

ACCEPTED MANUSCRIPT

## Conclusion

Azimuthal anisotropy within the Tibetan Plateau is evident from polarity switches with back-azimuth for the transverse RFs from the ASCENT deployment of 35 portable seismic stations. We infer both 2-lobed and 4-lobed back-azimuth patterns in Ps converted-wave amplitude, corresponding to dipping-axis and horizontal-axis anisotropy, respectively. Strong anisotropic signals are seen at delay times of 6-7 s and less, consistent with highly-sheared layers within the crust. Weak evidence for anisotropy is observed in the lowermost crust beneath the study region, which we infer to be composed of mafic granulite. We decompose the back-azimuth variation of RFs to exploit more information on anisotropic geometry. The main RF signals at shallow depths (0-2 s) display two-lobed variation with event back azimuth. Pronounced four-lobed RF variation at mid-lower crust is well recorded, suggesting horizontal or sub-horizontal axes.

Azimuthal anisotropy can be caused by aligned faults or parallel fractures in the upper crustal rocks, or by LPO of sheet micas or SPO of fluid disks in the mid-lower crust. Inversions are conducted by fitting the major phases on the harmonic RF stacks. Two-lobed and four-lobed RF patterns at the same arrival time are successfully explained by a single axis of symmetry. Our best-fitting models show the structure of two anisotropic zones at ~20-35 km and ~45-60 km with ~10%-15% anisotropy sandwiching an isotropic layer. Simple dynamic models have difficulty in explaining horizontal-axis anisotropy if we assume that mica or similar sheet silicates are the cause of anisotropy, because they would not easily be aligned vertically. We further hypothesize that the anisotropic zones in middle and lower crust represent vertically aligned tabular domains filled with fluids, minerals precipitated from fluid in vein networks, or else vertical chimneys of granulite-facies rocks with alternating hydration levels (e.g., amphibole content) related to channelization of metamorphic fluids. Our favored scenarios for Tibet-crust formation contrast with both the typical shortening and thickening model and underthrusting model. Our receiver-function estimates are most consistent with the intra-crustal pipe flow model, but the inferred

anisotropy is difficult to explain via kinematic models of rock strain. Our study may have detected the partial melting or dehydration caused by shear heating, and possibly large-scale vertical rock textures that develop during deep-crust metamorphism.

### Acknowledgement

We thank IRIS Data Management Center for providing us access to broadband seismograms recorded by ASCENT/INDEPTH-IV Network and China National Seismic Network. We also acknowledge useful conversations with Drs Yuri Podladchikov, Shun Karato, Erin Wirth, Tolulope Olugboji and Caroline Eakin.

## References

- Acton, C. E., Priestley, K., Gaur, V. K., Rai, S. S., 2010. Group velocity tomography of the Indo-Eurasian collision zone. *Journal of Geophysical Research: Solid Earth* 115(B12): B12335.
- Ague, J. J., 1994. Mass transfer during Barrovian metamorphism of pelites, south-central Connecticut; II, Channelized fluid flow and the growth of staurolite and kyanite. *American Journal of Science* 294(9): 1061-1134.
- Ague, J. J., 1995. Deep crustal growth of quartz, kyanite and garnet into large-aperture, fluid-filled fractures, northeastern Connecticut, USA. *Journal of Metamorphic Geology* 13(2): 299-314.
- Ague, J. J., 2003. Fluid Infiltration and Transport of Major, Minor, and Trace Elements During Regional Metamorphism of Carbonate Rocks, Wepawaug Schist, Connecticut, USA. *American Journal of Science* 303(9): 753-816.
- Allegre, C. J., Courtillot, V., Tapponnier, P., Hirn, A., Mattauer, M., Coulon, C., Jaeger, J. J., Achache, J., Scharer, U., Marcoux, J., Burg, J. P., Girardeau, J., Armijo, R., Gariépy, C., Gopel, C., Tindong, L., Xuchang, X., Chenfa, C., Guangqin, L., Baoyu, L., Jiwen, T., Naiwen, W., Guoming, C., Tonglin, H., Xibin, W., Wanming, D., Huaibin, S., Yougong, C., Ji, Z., Hongrong, Q., Peisheng, B., Songchan, W., Bixiang, W., Yaoxiu, Z., Xu, R., 1984. Structure and evolution of the Himalaya-Tibet orogenic belt. *Nature* 307(5946): 17-22.
- Bai, D., Unsworth, M. J., Meju, M. A., Ma, X., Teng, J., Kong, X., Sun, Y., Sun, J., Wang, L., Jiang, C., Zhao, C., Xiao, P., Liu, M., 2010. Crustal deformation of the eastern Tibetan plateau revealed by magnetotelluric imaging. *Nature Geosci* 3(5): 358-362.
- Barruol, G., Mainprice, D., 1993. A quantitative evaluation of the contribution of crustal rocks to the shear-wave splitting of teleseismic SKS waves. *Physics of the Earth and Planetary Interiors* 78(3-4): 281-300.
- Barruol, G., Kern, H., 1996. Seismic anisotropy and shear-wave splitting in lower-crustal and upper-mantle rocks from the Ivrea Zone—experimental and calculated data. *Physics of the Earth and Planetary Interiors* 95(3-4): 175-194.
- Beaumont, C., Jamieson, R. A., Nguyen, M. H., Medvedev, S., 2004. Crustal channel flows: 1. Numerical models with applications to the tectonics of the Himalayan-Tibetan orogen. *Journal of Geophysical Research: Solid Earth* 109(B6): B06406.
- Bianchi, I., Park, J., Piana Agostinetti, N., Levin, V., 2010. Mapping seismic anisotropy using harmonic decomposition of receiver functions: An application to Northern Apennines, Italy. *Journal of Geophysical Research: Solid Earth* 115(B12): B12317.

- Bohlen, S. R., Valley, J. W., Essene, E. J., 1985. Metamorphism in the Adirondacks. I. Petrology, Pressure and Temperature. *Journal of Petrology* 26(4): 971-992.
- Breeding, C. M., Ague, J. J., 2002. Slab-derived fluids and quartz-vein formation in an accretionary prism, Otago Schist, New Zealand. *Geology* 30(6): 499-502.
- Christensen, N. I., Fountain, D. M., 1975. Constitution of the Lower Continental Crust Based on Experimental Studies of Seismic Velocities in Granulite. *Geological Society of America Bulletin* 86(2): 227-236.
- Clark, M. K., Royden, L. H., 2000. Topographic ooze: Building the eastern margin of Tibet by lower crustal flow. *Geology* 28(8): 703-706.
- Connolly, J. A. D., Podladchikov, Y. Y., 2004. Fluid flow in compressive tectonic settings: Implications for midcrustal seismic reflectors and downward fluid migration. *Journal of Geophysical Research: Solid Earth* 109(B4): B04201.
- Connolly, J. A. D., Podladchikov, Y. Y., 2013. A Hydromechanical Model for Lower Crustal Fluid Flow. *Metasomatism and the Chemical Transformation of Rock*, Springer Berlin Heidelberg: 599-658.
- Crampin, S., Chastin, S., 2003. A review of shear wave splitting in the crack-critical crust. *Geophysical Journal International* 155(1): 221-240.
- Dash, J. G., Rempel, A. W., Wettlaufer, J. S., 2006. The physics of premelted ice and its geophysical consequences. *Reviews of Modern Physics* 78(3): 695-741.
- Dewey, J. F., Shackleton, R. M., Chengfa, C., Yiyin, S., 1988. The Tectonic Evolution of the Tibetan Plateau. *Philosophical Transactions of the Royal Society of London. Series A, Mathematical and Physical Sciences* 327(1594): 379-413.
- Dong, G., Mo, X., Zhao, Z., Guo, T., Wang, L., Chen, T., 2005. Geochronologic Constraints on the Magmatic Underplating of the Gangdisê Belt in the India-Eurasia Collision: Evidence of SHRIMP II Zircon U-Pb Dating. *Acta Geologica Sinica - English Edition* 79(6): 787-794.
- Dörr, W., Zulauf, G., 2010. Elevator tectonics and orogenic collapse of a Tibetan-style plateau in the European Variscides: the role of the Bohemian shear zone. *International Journal of Earth Sciences* 99(2): 299-325.
- Duret, F., Shapiro, N. M., Cao, Z., Levin, V., Molnar, P., Roecker, S., 2010. Surface wave dispersion across Tibet: Direct evidence for radial anisotropy in the crust. *Geophysical Research Letters* 37(16): L16306.
- England, P., Houseman, G., 1989. Extension during continental convergence, with application to the Tibetan Plateau. *Journal of Geophysical Research: Solid Earth* 94(B12): 17561-17579.

- Festa, A., Pini, G. A., Dilek, Y., Codegone, G., 2010. Mélanges and mélange-forming processes: a historical overview and new concepts. *International Geology Review* 52(10-12): 1040-1105.
- Fountain, D. M., 1989. Growth and modification of lower continental crust in extended terrains: the role of extension and magmatic underplating. Properties and processes of earth's lower crust: 287-299.
- Frederiksen, A. W., Bostock, M. G., 2000. Modelling teleseismic waves in dipping anisotropic structures. *Geophysical Journal International* 141(2): 401-412.
- Gray, R., Pysklywec, R. N., 2012. Geodynamic models of mature continental collision: Evolution of an orogen from lithospheric subduction to continental retreat/delamination. *Journal of Geophysical Research: Solid Earth* 117(B3): B03408.
- Guo, Z., Gao, X., Yao, H., Li, J., Wang, W., 2009. Midcrustal low-velocity layer beneath the central Himalaya and southern Tibet revealed by ambient noise array tomography. *Geochemistry, Geophysics, Geosystems* 10(5): Q05007.
- Healy, D., Reddy, S. M., Timms, N. E., Gray, E. M., Brovarone, A. V., 2009. Trench-parallel fast axes of seismic anisotropy due to fluid-filled cracks in subducting slabs. *Earth and Planetary Science Letters* 283(1-4): 75-86.
- Huang, H., Yao, H., van der Hilst, R. D., 2010. Radial anisotropy in the crust of SE Tibet and SW China from ambient noise interferometry. *Geophysical Research Letters* 37(21): L21310.
- Huang, W.-C., Ni, J. F., Tilmann, F., Nelson, D., Guo, J., Zhao, W., Mechie, J., Kind, R., Saul, J., Rapine, R., Hearn, T. M., 2000. Seismic polarization anisotropy beneath the central Tibetan Plateau. *Journal of Geophysical Research: Solid Earth* 105(B12): 27979-27989.
- Jackson, J., McKenzie, D., Priestley, K., Emmerson, B., 2008. New views on the structure and rheology of the lithosphere. *Journal of the Geological Society* 165(2): 453-465.
- Ji, S., Salisbury, M. H., 1993. Shear-wave velocities, anisotropy and splitting in high-grade mylonites. *Tectonophysics* 221(3-4): 453-473.
- Ji, S., Shao, T., Michibayashi, K., Long, C., Wang, Q., Kondo, Y., Zhao, W., Wang, H., Salisbury, M. H., 2013. A new calibration of seismic velocities, anisotropy, fabrics, and elastic moduli of amphibole-rich rocks. *Journal of Geophysical Research: Solid Earth* 118(9): 4699-4728.
- Jiang, M., Zhou, S., Sandvol, E., Chen, X., Liang, X., Chen, Y. J., Fan, W., 2011. 3-D lithospheric structure beneath southern Tibet from Rayleigh-wave tomography with a 2-D seismic array. *Geophysical Journal International* 185(2): 593-608.
- Kaneshima, S., 1990. Origin of crustal anisotropy: Shear Wave splitting studies in Japan. *Journal of Geophysical Research: Solid Earth* 95(B7): 11121-11133.
- Karato, S.-i., 2012. On the origin of the asthenosphere. *Earth and Planetary Science Letters* 321-



- 322(0): 95-103.
- Kê, T. i.-S., 1947. Experimental Evidence of the Viscous Behavior of Grain Boundaries in Metals. *Physical Review* 71(8): 533-546.
- Kendall, J., 2000. Seismic anisotropy in the boundary layers of the mantle. *Earth's Deep Interior: Mineral physics and tomography from the atomic to the global scale*: 133-159.
- Kendall, J. M., Silver, P. G., 1996. Constraints from Seismic Anisotropy on the Nature of the Lowermost Mantle. *Nature* 381(6581): 409-412.
- Kern, H., Wenk, H. R., 1990. Fabric-related velocity anisotropy and shear wave splitting in rocks from the Santa Rosa Mylonite Zone, California. *Journal of Geophysical Research: Solid Earth* 95(B7): 11213-11223.
- Kind, R., Ni, J., Zhao, W., Wu, J., Yuan, X., Zhao, L., Sandvol, E., Reese, C., Nabelek, J., Hearn, T., 1996. Evidence from Earthquake Data for a Partially Molten Crustal Layer in Southern Tibet. *Science* 274(5293): 1692-1694.
- Kind, R., Yuan, X., Saul, J., Nelson, D., Sobolev, S. V., Mechie, J., Zhao, W., Kosarev, G., Ni, J., Achauer, U., Jiang, M., 2002. Seismic Images of Crust and Upper Mantle Beneath Tibet: Evidence for Eurasian Plate Subduction. *Science* 298(5596): 1219-1221.
- Kirby, S. H., 1984. Introduction and digest to the Special Issue on Chemical Effects of Water on the Deformation and Strengths of Rocks. *Journal of Geophysical Research: Solid Earth* 89(B6): 3991-3995.
- Klemperer, S. L., 2006. Crustal flow in Tibet: geophysical evidence for the physical state of Tibetan lithosphere, and inferred patterns of active flow. *Geological Society, London, Special Publications* 268(1): 39-70.
- Krystopowicz, N. J., Currie, C. A., 2013. Crustal eclogitization and lithosphere delamination in orogens. *Earth and Planetary Science Letters* 361(0): 195-207.
- Lee, L. C., Morris, S. J. S., 2010. Anelasticity and grain boundary sliding. *Proceedings of the Royal Society of London A: Mathematical, Physical and Engineering Sciences*.
- Lei, J., Li, Y., Xie, F., Teng, J., Zhang, G., Sun, C., Zha, X., 2014. Pn anisotropic tomography and dynamics under eastern Tibetan plateau. *Journal of Geophysical Research: Solid Earth* 119(3): 2013JB010847.
- Lev, E., Long, M. D., van der Hilst, R. D., 2006. Seismic anisotropy in Eastern Tibet from shear wave splitting reveals changes in lithospheric deformation. *Earth and Planetary Science Letters* 251(3-4): 293-304.
- Levin, V., Park, J., 1997a. P-SH conversions in a flat-layered medium with anisotropy of arbitrary orientation. *Geophysical Journal International* 131(2): 253-266.

- Levin, V., Park, J., 1997b. Crustal anisotropy in the Ural Mountains Foredeep from teleseismic receiver functions. *Geophysical Research Letters* 24(11): 1283-1286.
- Levin, V., Park, J., 1998. P-SH Conversions in Layered Media with Hexagonally Symmetric Anisotropy: A CookBook. *Geodynamics of Lithosphere & Earth's Mantle*. J. Plomerová, R. Liebermann, V. Babuška, Birkhäuser Basel: 669-697.
- Levin, V., Park, J., 2000. Shear zones in the Proterozoic lithosphere of the Arabian Shield and the nature of the Hales discontinuity. *Tectonophysics* 323(3-4): 131-148.
- Li, H., Su, W., Wang, C.-Y., Huang, Z., 2009. Ambient noise Rayleigh wave tomography in western Sichuan and eastern Tibet. *Earth and Planetary Science Letters* 282(1-4): 201-211.
- Liu, H., Niu, F., 2012. Estimating crustal seismic anisotropy with a joint analysis of radial and transverse receiver function data. *Geophysical Journal International* 188(1): 144-164.
- Long, M. D., 2013. Constraints on subduction geodynamics from seismic anisotropy. *Reviews of Geophysics* 51(1): 76-112.
- Maupin, V., Park, J., 2007. Theory and observations—wave propagation in anisotropic media. *Seismology and the Structure of the Earth. Treatise on Geophysics* 1: 289-321.
- McKenzie, D., Priestley, K., 2008. The influence of lithospheric thickness variations on continental evolution. *Lithos* 102(1-2): 1-11.
- McLelland, J. M., 1984. The origin of ribbon lineation within the southern Adirondacks, U.S.A. *Journal of Structural Geology* 6(1-2): 147-157.
- McLelland, J. M., Selleck, B. W., 2011. Megacrystic Gore Mountain-type garnets in the Adirondack Highlands: Age, origin, and tectonic implications. *Geosphere* 7(5): 1194-1208.
- McNamara, D. E., Owens, T. J., Silver, P. G., Wu, F. T., 1994. Shear wave anisotropy beneath the Tibetan Plateau. *Journal of Geophysical Research: Solid Earth* 99(B7): 13655-13665.
- Nábělek, J., Hetényi, G., Vergne, J., Sapkota, S., Kafle, B., Jiang, M., Su, H., Chen, J., Huang, B.-S., Team, t. H.-C., 2009. Underplating in the Himalaya-Tibet Collision Zone Revealed by the Hi-CLIMB Experiment. *Science* 325(5946): 1371-1374.
- Nelson, K. D., Zhao, W., Brown, L. D., Kuo, J., Che, J., Liu, X., Klemperer, S. L., Makovsky, Y., Meissner, R., Mechie, J., Kind, R., Wenzel, F., Ni, J., Nabelek, J., Leshou, C., Tan, H., Wei, W., Jones, A. G., Booker, J., Unsworth, M., Kidd, W. S. F., Hauck, M., Alsdorf, D., Ross, A., Cogan, M., Wu, C., Sandvol, E., Edwards, M., 1996. Partially Molten Middle Crust Beneath

- Southern Tibet: Synthesis of Project INDEPTH Results. *Science* 274(5293): 1684-1688.
- Nikulin, A., Levin, V., Park, J., 2009. Receiver function study of the Cascadia megathrust: Evidence for localized serpentinization. *Geochemistry, Geophysics, Geosystems* 10(7): Q07004.
- O'Rourke, J. G., Korenaga, J., 2012. Terrestrial planet evolution in the stagnant-lid regime: Size effects and the formation of self-destabilizing crust. *Icarus* 221(2): 1043-1060.
- Okaya, D. A., Christensen, N. I., 2002. Anisotropic effects of non-axial seismic wave propagation in foliated crustal rocks. *Geophysical Research Letters* 29(11): 2-1-2-4.
- Olugboji, T. M., Karato, S., Park, J., 2013. Structures of the oceanic lithosphere-asthenosphere boundary: Mineral-physics modeling and seismological signatures. *Geochemistry, Geophysics, Geosystems* 14(4): 880-901.
- Orville, P. M., 1969. A model for metamorphic differentiation origin of thin-layered amphibolites. *American Journal of Science* 267(1): 64-86.
- Ozacar, A. A., Zandt, G., 2004. Crustal seismic anisotropy in central Tibet: Implications for deformational style and flow in the crust. *Geophysical Research Letters* 31(23): L23601.
- Park, J., Lindberg, C. R., Vernon, F. L., 1987. Multitaper spectral analysis of high-frequency seismograms. *Journal of Geophysical Research: Solid Earth* 92(B12): 12675-12684.
- Park, J., Levin, V., 2000. Receiver Functions from Multiple-Taper Spectral Correlation Estimates. *Bulletin of the Seismological Society of America* 90(6): 1507-1520.
- Park, J., Levin, V., 2002. Seismic Anisotropy: Tracing Plate Dynamics in the Mantle. *Science* 296(5567): 485-489.
- Park, J., Yuan, H., Levin, V., 2004. Subduction zone anisotropy beneath Corvallis, Oregon: A serpentinite skid mark of trench-parallel terrane migration? *Journal of Geophysical Research: Solid Earth* 109(B10): B10306.
- Patiño Douce, A., McCarthy, T. C., 1998. Melting of Crustal Rocks During Continental Collision and Subduction. *When Continents Collide: Geodynamics and Geochemistry of Ultrahigh-Pressure Rocks*. B. Hacker, J. Liou, Springer Netherlands. **10**: 27-55.
- Peng, X., Humphreys, E. D., 1997. Moho dip and crustal anisotropy in northwestern Nevada from teleseismic receiver functions. *Bulletin of the Seismological Society of America* 87(3): 745-754.
- Royden, L. H., Burchfiel, B. C., King, R. W., Wang, E., Chen, Z., Shen, F., Liu, Y., 1997. Surface Deformation and Lower Crustal Flow in Eastern Tibet. *Science* 276(5313): 788-790.

- Rubin, A. M., 1995. Propagation of Magma-Filled Cracks. *Annual Review of Earth and Planetary Sciences* 23(1): 287-336.
- Rudnick, R. L., Fountain, D. M., 1995. Nature and composition of the continental crust: A lower crustal perspective. *Reviews of Geophysics* 33(3): 267-309.
- Savage, M. K., 1998. Lower crustal anisotropy or dipping boundaries? Effects on receiver functions and a case study in New Zealand. *Journal of Geophysical Research: Solid Earth* 103(B7): 15069-15087.
- Savage, M. K., Park, J., Todd, H., 2007. Velocity and anisotropy structure at the Hikurangi subduction margin, New Zealand from receiver functions. *Geophysical Journal International* 168(3): 1034-1050.
- Shapiro, N. M., Ritzwoller, M. H., Molnar, P., Levin, V., 2004. Thinning and Flow of Tibetan Crust Constrained by Seismic Anisotropy. *Science* 305(5681): 233-236.
- Shea Jr, W. T., Kronenberg, A. K., 1993. Strength and anisotropy of foliated rocks with varied mica contents. *Journal of Structural Geology* 15(9-10): 1097-1121.
- Sherrington, H. F., Zandt, G., Frederiksen, A., 2004. Crustal fabric in the Tibetan Plateau based on waveform inversions for seismic anisotropy parameters. *Journal of Geophysical Research: Solid Earth* 109(B2): B02312.
- Shiomi, K., Park, J., 2008. Structural features of the subducting slab beneath the Kii Peninsula, central Japan: Seismic evidence of slab segmentation, dehydration, and anisotropy. *Journal of Geophysical Research: Solid Earth* 113(B10): B10318.
- Siegesmund, S., Kern, H., 1990. Velocity anisotropy and shear-wave splitting in rocks from the mylonite belt along the Insubric Line (Ivrea Zone, Italy). *Earth and Planetary Science Letters* 99(1-2): 29-47.
- Skjerlie, K. P., Patiño Douce, A. E., 2002. The Fluid-absent Partial Melting of a Zoisite-bearing Quartz Eclogite from 1.0 to 3.2 GPa; Implications for Melting in Thickened Continental Crust and for Subduction-zone Processes. *Journal of Petrology* 43(2): 291-314.
- Sun, Y., Niu, F., Liu, H., Chen, Y., Liu, J., 2012. Crustal structure and deformation of the SE Tibetan plateau revealed by receiver function data. *Earth and Planetary Science Letters* 349-350(0): 186-197.
- Tandon, G. P., Weng, G. J., 1984. The effect of aspect ratio of inclusions on the elastic properties of unidirectionally aligned composites. *Polymer Composites* 5(4): 327-333.
- Taylor, M., Yin, A., 2009. Active structures of the Himalayan-Tibetan orogen and their relationships to earthquake distribution, contemporary strain field, and Cenozoic volcanism. *Geosphere* 5(3): 199-214.

- Thompson, A. B., Connolly, J. A. D., 1995. Melting of the continental crust: Some thermal and petrological constraints on anatexis in continental collision zones and other tectonic settings. *Journal of Geophysical Research: Solid Earth* 100(B8): 15565-15579.
- Thomson, D. J., 1982. Spectrum estimation and harmonic analysis. *Proceedings of the IEEE* 70(9): 1055-1096.
- Unsworth, M., Wenbo, W., Jones, A. G., Li, S., Bedrosian, P., Booker, J., Sheng, J., Ming, D., Handong, T., 2004. Crustal and upper mantle structure of northern Tibet imaged with magnetotelluric data. *Journal of Geophysical Research: Solid Earth* 109(B2): B02403.
- Valley, J. W., Bohlen, S. R., Essene, E. J., Lamb, W., 1990. Metamorphism in the Adirondacks: II. The Role of Fluids. *Journal of Petrology* 31(3): 555-596.
- Vergne, J., Wittlinger, G., Hui, Q., Tapponnier, P., Poupinet, G., Mei, J., Herquel, G., Paul, A., 2002. Seismic evidence for stepwise thickening of the crust across the NE Tibetan plateau. *Earth and Planetary Science Letters* 203(1): 25-33.
- Volland, S., Kruhl, J. H., 2004. Anisotropy quantification: the application of fractal geometry methods on tectonic fracture patterns of a Hercynian fault zone in NW Sardinia. *Journal of Structural Geology* 26(8): 1499-1510.
- Wei, W., Unsworth, M., Jones, A., Booker, J., Tan, H., Nelson, D., Chen, L., Li, S., Solon, K., Bedrosian, P., Jin, S., Deng, M., Ledo, J., Kay, D., Roberts, B., 2001. Detection of Widespread Fluids in the Tibetan Crust by Magnetotelluric Studies. *Science* 292(5517): 716-719.
- Wettlaufer, J. S., 1999. Impurity Effects in the Premelting of Ice. *Physical Review Letters* 82(12): 2516-2519.
- Whitney, D. L., Teyssier, C., Fayon, A. K., 2004. Isothermal decompression, partial melting and exhumation of deep continental crust. *Geological Society, London, Special Publications* 227(1): 313-326.
- Willet, S. D., Beaumont, C., 1994. Subduction of Asian lithospheric mantle beneath Tibet inferred from models of continental collision. *Nature* 369(6482): 642-645.
- Williams, Q., Garnero, E. J., 1996. Seismic Evidence for Partial Melt at the Base of Earth's Mantle. *Science* 273(5281): 1528-1530.
- Wirth, E. A., Long, M. D., 2012. Multiple layers of seismic anisotropy and a low-velocity region in the mantle wedge beneath Japan: Evidence from teleseismic receiver functions. *Geochemistry, Geophysics, Geosystems* 13(8): Q08005.
- Wirth, E. A., Long, M. D., 2014. A contrast in anisotropy across mid-lithospheric discontinuities beneath the central United States—A relic of craton formation. *Geology* 42(10): 851-854.
- Xie, J., Ritzwoller, M. H., Shen, W., Yang, Y., Zheng, Y., Zhou, L., 2013. Crustal radial

- anisotropy across Eastern Tibet and the Western Yangtze Craton. *Journal of Geophysical Research: Solid Earth* 118(8): 4226-4252.
- Xu, L., Rondenay, S., van der Hilst, R. D., 2007. Structure of the crust beneath the southeastern Tibetan Plateau from teleseismic receiver functions. *Physics of the Earth and Planetary Interiors* 165(3–4): 176-193.
- Xu, Q., Zhao, J., Pei, S., Liu, H., 2013. Imaging lithospheric structure of the eastern Himalayan syntaxis: New insights from receiver function analysis. *Journal of Geophysical Research: Solid Earth* 118(5): 2323-2332.
- Yakovlev, P. V., Clark, M. K., 2014. Conservation and redistribution of crust during the Indo-Asian collision. *Tectonics* 33(6): 2013TC003469.
- Yang, Y., Zheng, Y., Chen, J., Zhou, S., Ceylan, S., Sandvol, E., Tilmann, F., Priestley, K., Hearn, T. M., Ni, J. F., Brown, L. D., Ritzwoller, M. H., 2010. Rayleigh wave phase velocity maps of Tibet and the surrounding regions from ambient seismic noise tomography. *Geochemistry, Geophysics, Geosystems* 11(8): Q08010.
- Yang, Y., Ritzwoller, M. H., Zheng, Y., Shen, W., Levshin, A. L., Xie, Z., 2012. A synoptic view of the distribution and connectivity of the mid-crustal low velocity zone beneath Tibet. *Journal of Geophysical Research: Solid Earth* 117(B4): B04303.
- Yao, H., Beghein, C., Van Der Hilst, R. D., 2008. Surface wave array tomography in SE Tibet from ambient seismic noise and two-station analysis - II. Crustal and upper-mantle structure. *Geophysical Journal International* 173(1): 205-219.
- Yin, A., Harrison, T. M., 2000. Geologic Evolution of the Himalayan-Tibetan Orogen. *Annual Review of Earth and Planetary Sciences* 28(1): 211-280.
- Yue, H., Chen, Y. J., Sandvol, E., Ni, J., Hearn, T., Zhou, S., Feng, Y., Ge, Z., Trujillo, A., Wang, Y., Jin, G., Jiang, M., Tang, Y., Liang, X., Wei, S., Wang, H., Fan, W., Liu, Z., 2012. Lithospheric and upper mantle structure of the northeastern Tibetan Plateau. *Journal of Geophysical Research: Solid Earth* 117(B5): B05307.
- Zhao, W.-L., Morgan, W. J., 1987. Injection of Indian crust into Tibetan lower crust: A two-dimensional finite element model study. *Tectonics* 6(4): 489-504.

## Captions

**Figure 1.** Map of selected stations (triangles) from ASCENT network plotted against topography. Red triangles are stations we choose for forward modeling. Major geological structures (dashed lines) are plotted using HimaTibetMap database (Taylor and Yin, 2009). KF: Kunlun Fault, JS: Jinsha Suture, BNS: Bangong-Nujiang Suture, IZS: Indus-Zangbo Suture.

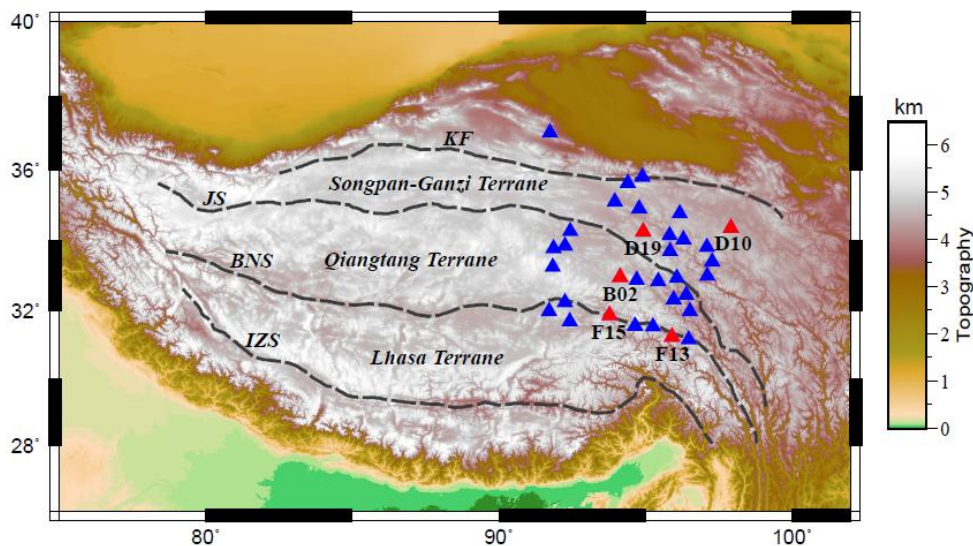


**Figure 2.** An azimuthal equidistant map of seismic events centered at ( $95^{\circ}$ ,  $34^{\circ}$ ). Epicentral distances (numbers) are indicated by concentric circles. Red stars show earthquake locations. Blue triangles are seismic stations. Events between two green lines ( $110^{\circ}$ - $135^{\circ}$ ) are further used for epicentral distance RF sweep.

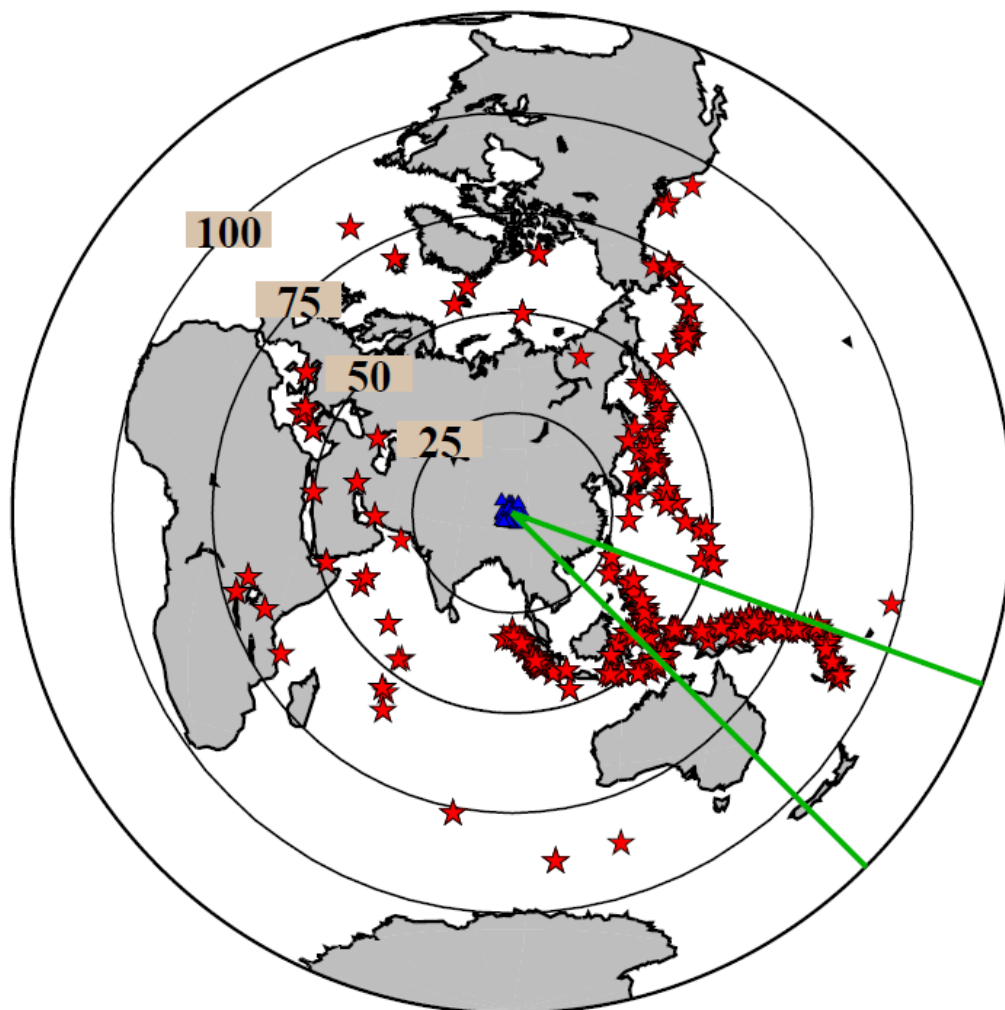




**Figure 3.** Back-azimuth RF sweep (a) and harmonic expansion terms (b) of station X4F13; In (a), the green curve outlines the arrivals of Pms phases. The vertical red line denotes zero delay time. Yellow and green shadings highlight the crustal Ps phases at ~2-4 s and ~4.5-7 s, respectively. Stars mark the occurrence of polarity reversals. Radial and transverse RFs are plotted in the same scale. The “dip/anisotropy” and “unmodelled” panels are plotted in the same scale.

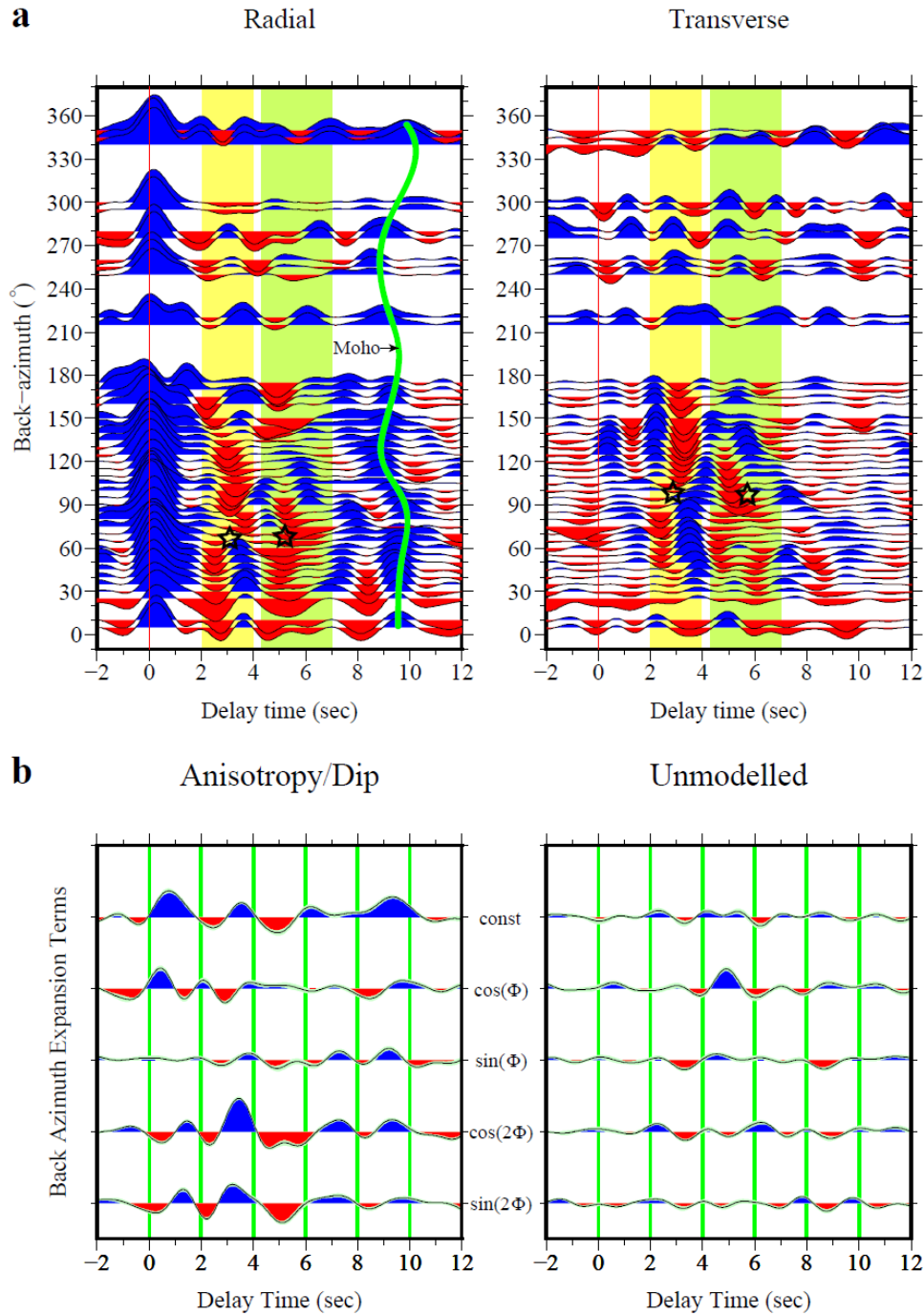


**Figure 4.** A comparison of epicentral-distance RF sweeps between real (a) and synthetic (b) X4F13 data. In (a), the green, purple and orange line highlights the Moho discontinuity, a lower crustal interface and near surface interface, respectively. In (b), Moho arrivals with a negative moveout are indicated by green line. Signals at ~2-4 s (dashed and black lines) are multiple phases from the interface at ~0.5 s. By comparing (a) and (b), the negative pulses at ~2-4 s (black curve) in (a) are not interpreted to be reverberated phases for missing equally strong positive pulses that are outlined by the dashed black line in (b).

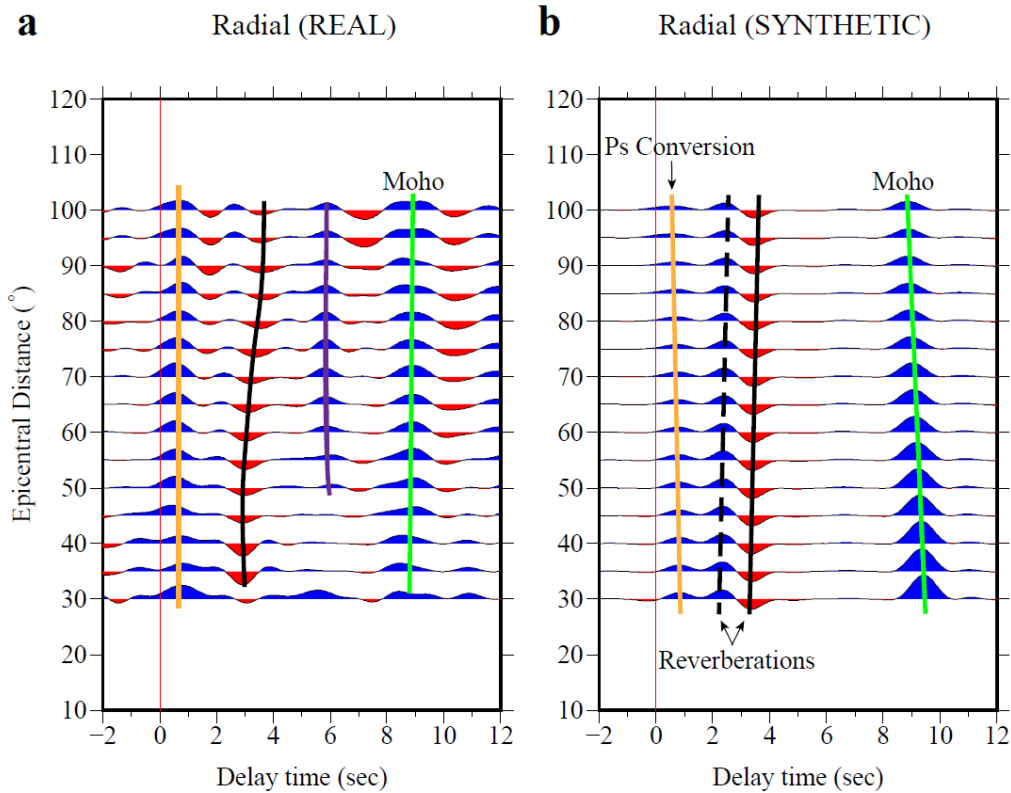


**Figure 5.** Back-azimuth RF sweep (a) and harmonic expansion terms (b) of station X4F15; In (a), the green curve outlines the arrivals of Pms phases. The vertical red line denotes zero delay time. Yellow and green shadings highlight the crustal Ps phases at ~2-4 s and ~5-6.5 s, respectively. Stars mark the occurrence of polarity reversals. Radial and transverse RFs are plotted in the same scale. The “dip/anisotropy” and “unmodelled” panels are plotted in the same scale.

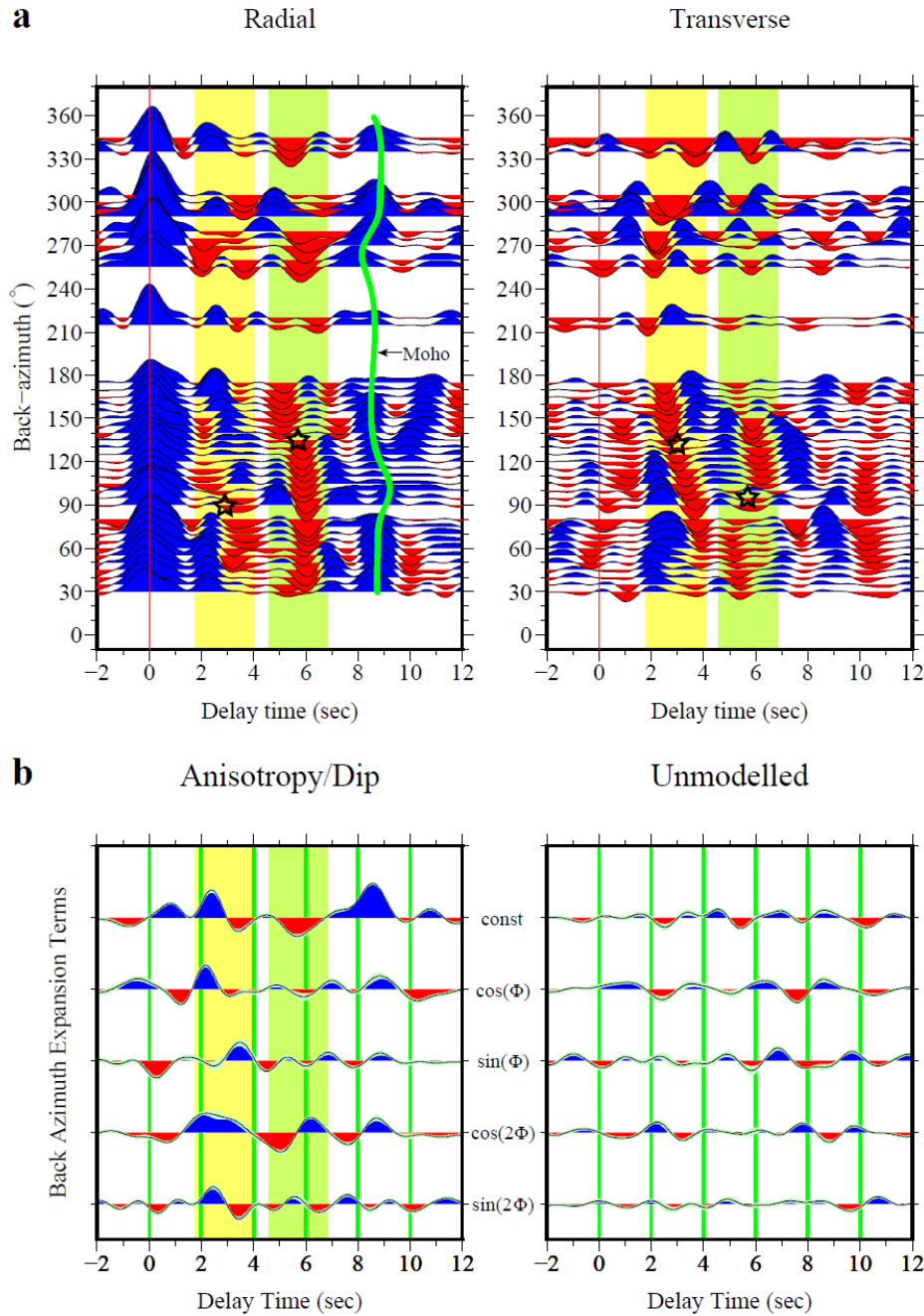


**Figure 6.** Back-azimuth RF sweep (a) and harmonic expansion terms (b) of station X4D19; In (a), the green curve outlines the arrivals of Pms phases. The vertical red line denotes zero delay time. Yellow and green shadings highlight the crustal Ps phases at ~2-4 s and ~5-6.5 s, respectively. Stars mark the occurrence of polarity reversals. Radial and transverse RFs are plotted in the same scale. The “dip/anisotropy” and “unmodelled” panels are plotted in the same scale.

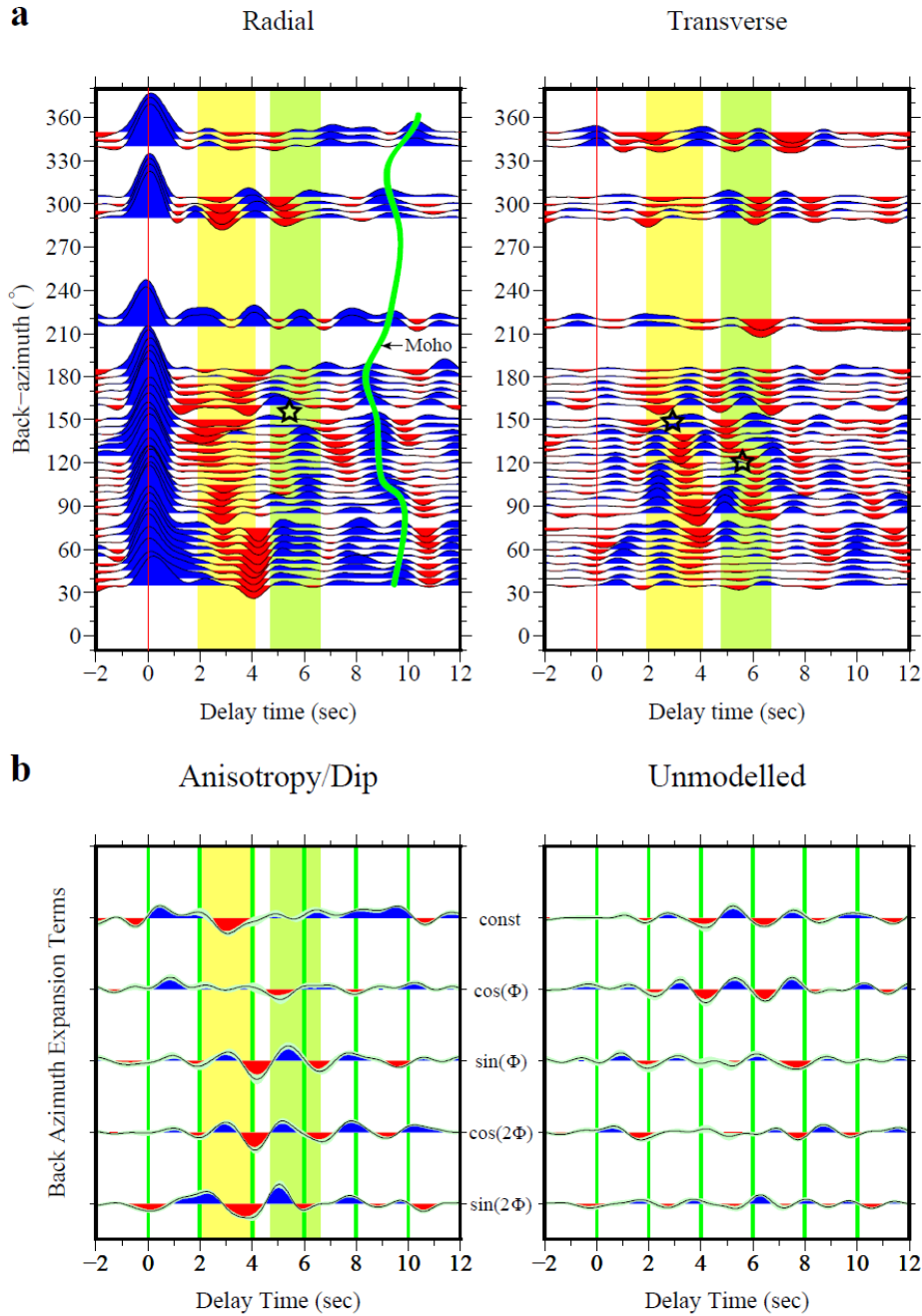


**Figure 7.** X4F13 anisotropic velocity model estimated from forward-modeling inversions. Blue region indicates the anisotropic layer.  $\delta$  and  $\theta$  are the plunge and strike of the symmetry axis, respectively. P.A. is the percent anisotropy assigned to the layer. A negative value of P.A. means that the unique axis is a slow axis and vice versa.  $V_p/V_s$  ratio is fixed at 1.80.

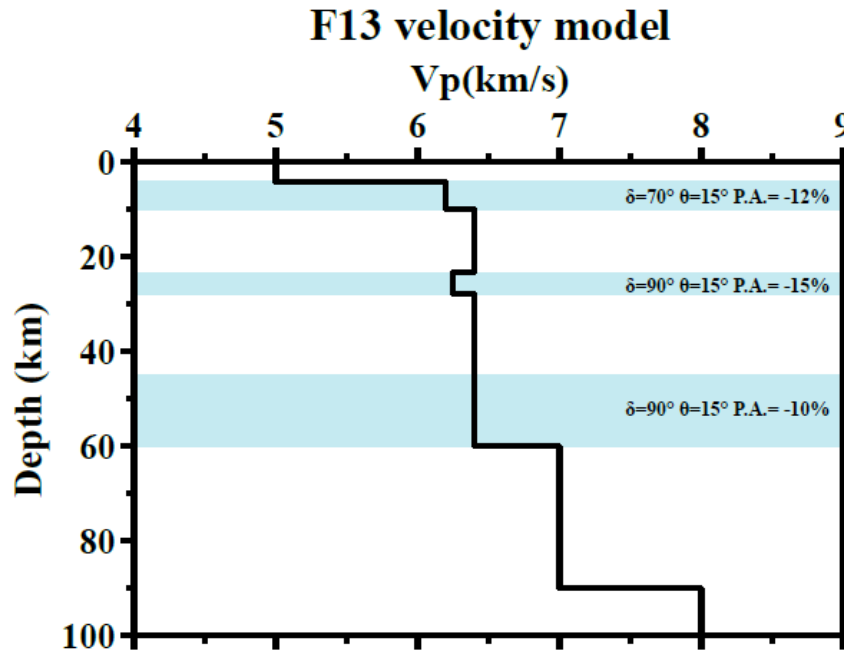


**Figure 8.** Synthetic (red) and real (black) harmonic stacks (“dip/anisotropy” part) plotted in the same scale for X4F13; Numbers below each trace annotation are cross-correlation coefficients (zero lag) of the real series and synthetic series of each term. High values indicate that the data has been well fit.

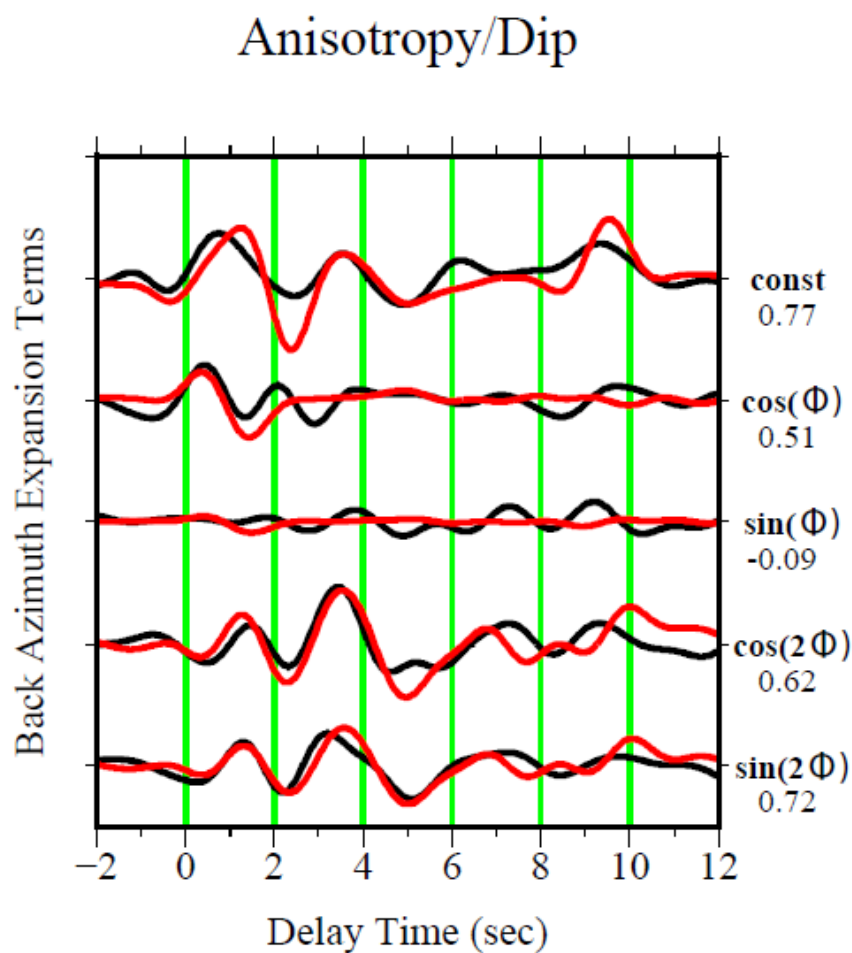


**Figure 9.** X4F15 anisotropic velocity model estimated from forward-modeling inversions. Blue region indicates the anisotropic layer.  $\delta$  and  $\theta$  are the plunge and strike of the symmetry axis, respectively. P.A. is the percent anisotropy assigned to the layer. A negative value of P.A. means that the unique axis is a slow axis and vice versa.  $V_p/V_s$  ratio is fixed at 1.80.

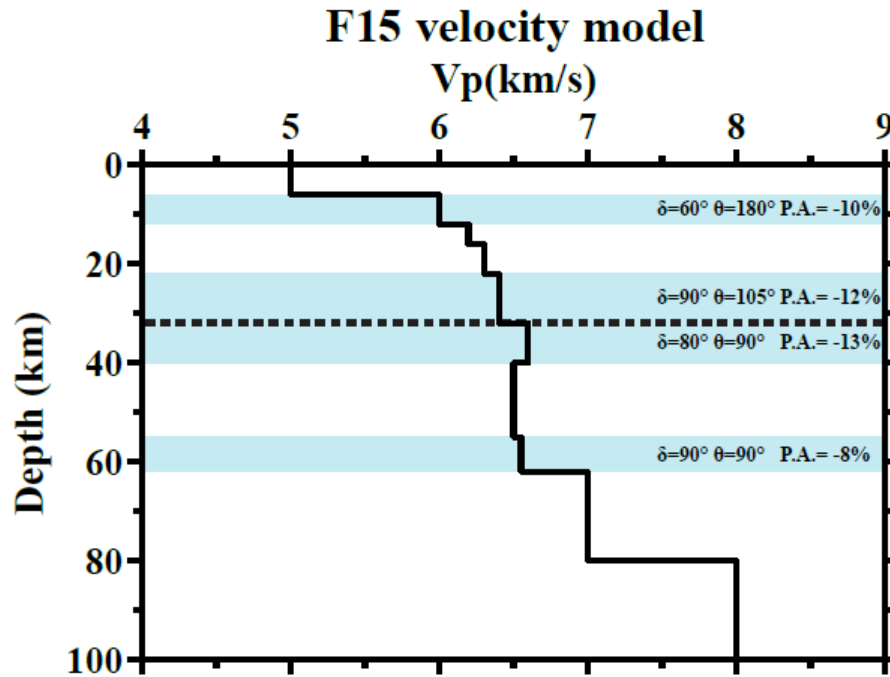


**Figure 10.** Synthetic (red) and real (black) harmonic stacks (“dip/anisotropy” part) plotted in the same scale for X4F15; Numbers below each trace annotation are cross-correlation coefficients (zero lag) of the real series and synthetic series of each term. High values indicate that the data has been well fit.

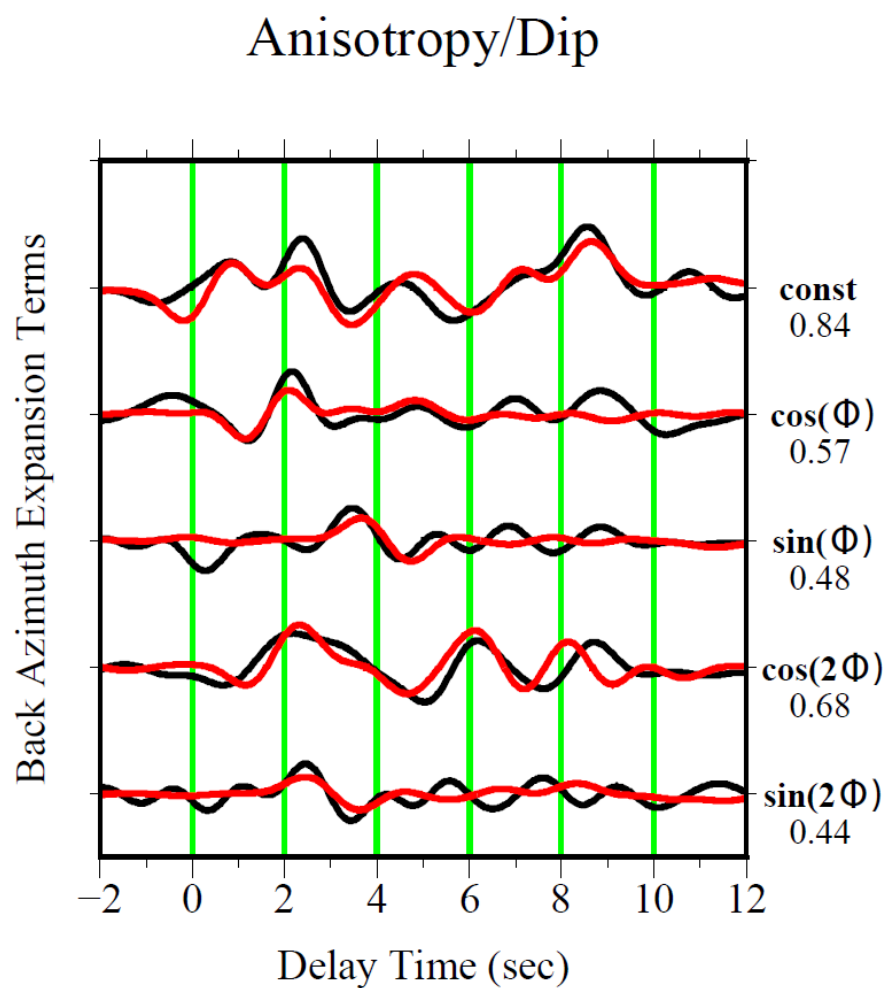




**Figure 11.** X4D19 anisotropic velocity model estimated from forward-modeling inversions. Blue region indicates the anisotropic layer. The dashed line separates two anisotropic layers with similar symmetry orientations.  $\delta$  and  $\theta$  are the plunge and strike of the symmetry axis, respectively. P.A. is the percent anisotropy assigned to the layer. A negative value of P.A. means that the unique axis is a slow axis and vice versa.  $V_p/V_s$  ratio is fixed at 1.80.

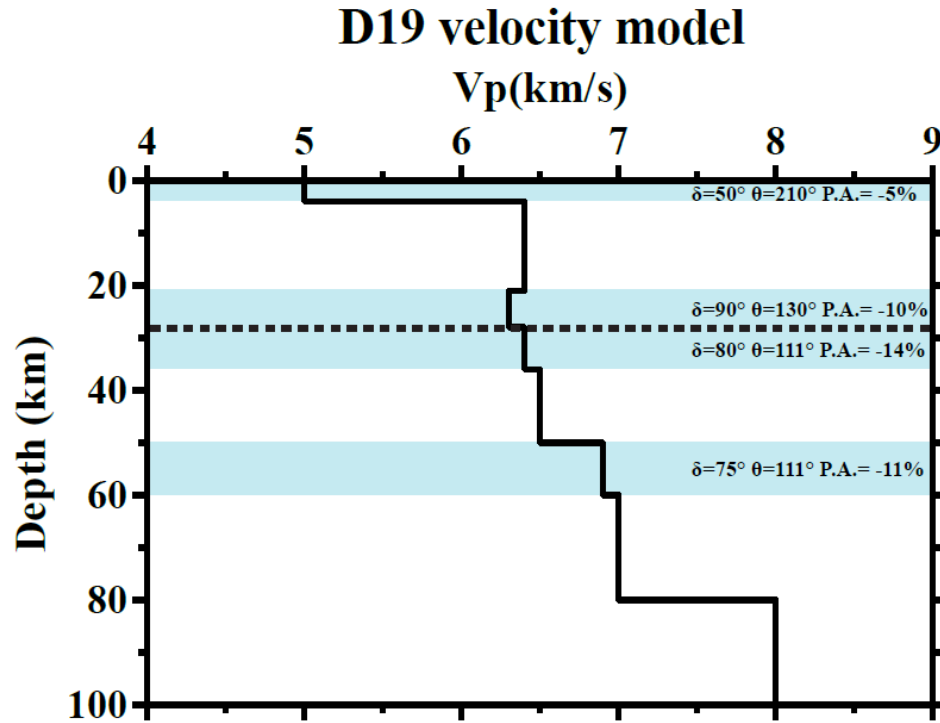


**Figure 12.** Synthetic (red) and real (black) harmonic stacks (“dip/anisotropy” part) plotted in the same scale for X4D19; Numbers below each trace annotation are cross-correlation coefficients (zero lag) of the real series and synthetic series of each term. High values indicate that the data has been well fit.

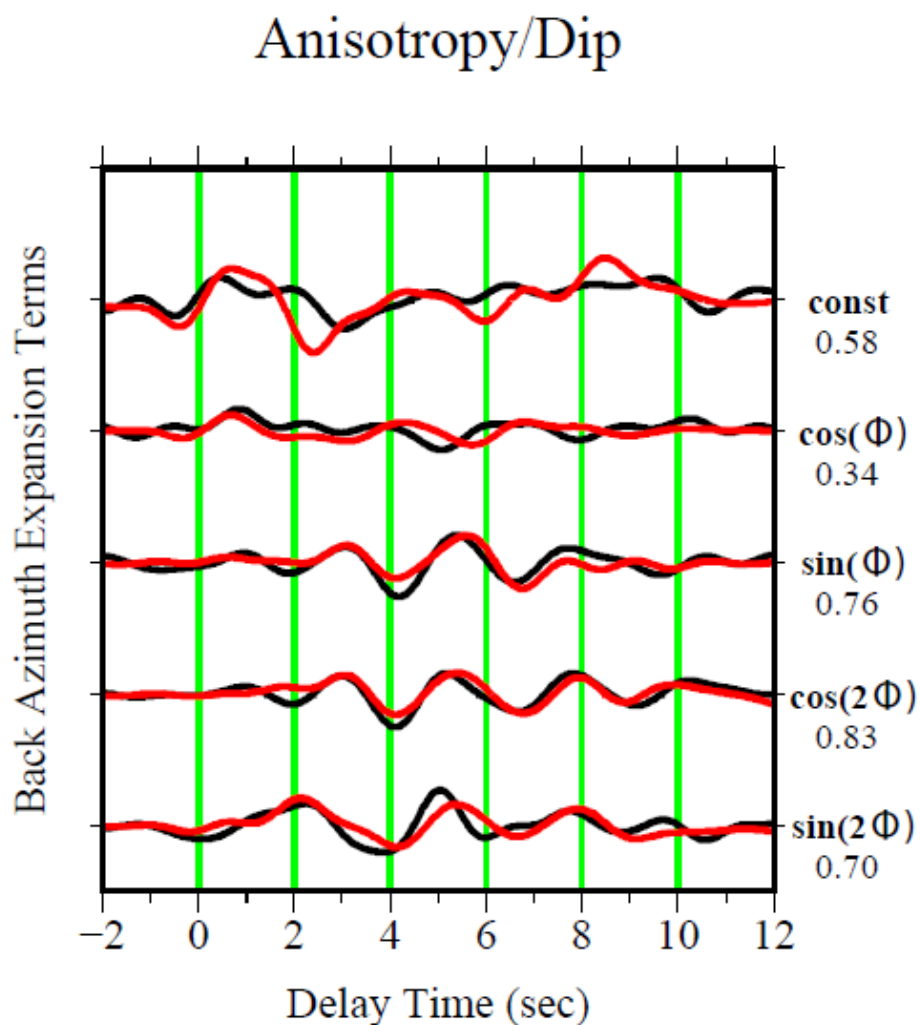
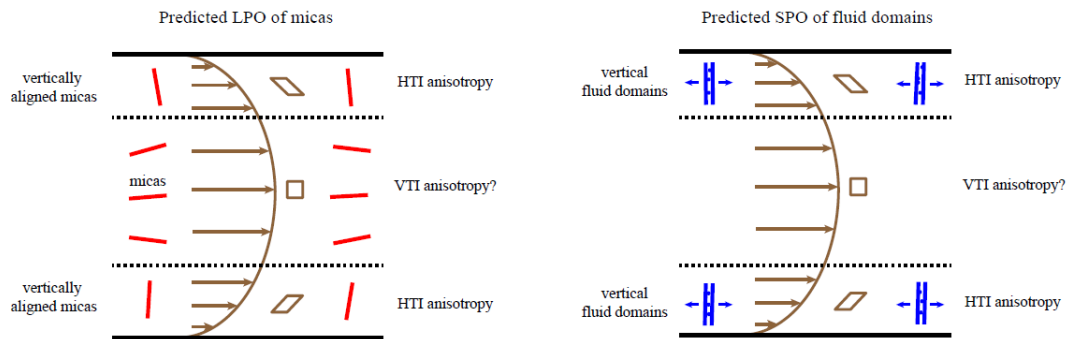


**Figure 13.** LPO of micas (a) and SPO of fluid domains (b) predicted by RF data. Vertically aligned micas or tabular fluid domains are required to generate horizontal slow axis. Brown curve depicts the velocity gradient of pipe flow. Parallelograms and squares indicate the maximum shear and weak shear, respectively. HTI: horizontal transverse isotropy; VTI: vertical transverse isotropy. The azimuthally isotropic layer in the middle could be caused by horizontally located micas grains in (a) or the absence of SPO in (b). Geometry of the sandwich-like mid-to-lower crustal structure is coincident with the structure of pipe flow.



### Highlights

- (1) We analyzed 35 stations using receiver-functions and forward-modeled five stations
- (2) Anisotropy concentrates in three isolated zones in the upper, middle and lower crust
- (3) Horizontal symmetry axes are inconsistent with typical LPO of foliated crustal rocks
- (4) LPO of metamorphic veins or channelized metamorphic are alternative explanations